Joint Downlink Wireless Energy Delivery-Uplink Data Reporting Design for System Energy Efficiency in Active IRS-Aided CRSNs

Jihong WANG[1], Qiang XU[1], Yanan ZHU[1], Yang LI[1],
Ikromjon Usmonovichb RAKHMONOV[2], Kahramon Rakhimovichb ALLAEV [2],

[1] School of Electrical Engineering, Northeast Electric Power University, Jilin, 132012, China
[2] Department of Power Supply, Tashkent State Technical University, Tashkent, 100095, Uzbekistan

wangjihong@neepu.edu.cn, xuqiang250906@163.com, zhuyanan106@126.com, liyang@neepu.edu.cn, raxmonov.ikromjon@tdtu.uz, kahramon-allaev@mail.ru

Submitted July 12, 2026 / Accepted November 5, 2026 / Online first November 20, 2026

Abstract. *Active intelligent reflecting surfaces (AIRSs) can simultaneously enhance downlink wireless energy delivery (DWED) and uplink data reporting (UDR) in energy-harvesting cognitive radio sensor networks (EH-CRSNs). Different from our previous node-side net-energy-gain-oriented study, this work investigates a multi-antenna AIRS-aided EH-CRSN from a system-level energy-efficiency (EE) perspective. A unified energy-consumption model is developed by jointly accounting for the power consumption of the sink, CRSN nodes, and AIRS. The DWED transmit beamformer, UDR receive beamformer, and AIRS reflection-coefficient matrices for the downlink and uplink phases are jointly optimized to maximize the system EE under the sink transmit-power and AIRS amplification-power constraints. The resulting non-convex problem is solved using an alternating-optimization framework combining successive convex approximation and semidefinite relaxation. To explore the fundamental performance limits of the proposed AIRS-aided EH-CRSN EE, the instantaneous channel state information is assumed to be known in the derivation of the optimization algorithm. Numerical results demonstrate that the proposed scheme achieves higher system EE than the benchmark schemes while maintaining the reduction in the residual energy of CRSN nodes within 1.2%. The results also show that increasing the number of active reflecting elements or the AIRS amplification-power budget does not always improve the system EE due to the additional power consumption of active reflection. Whether under Rayleigh or Rician fading channels, the proposed scheme consistently yields superior system EE over existing baseline schemes.*

Keywords

Active intelligent reflecting surface, cognitive radio sensor networks, energy efficiency, energy harvesting

1. Introduction

Energy-harvesting cognitive radio sensor networks (EH-CRSNs) integrate radio frequency (RF) EH capability into CRSNs to mitigate the lifetime limitation caused by the restricted energy supply of sensor nodes [1]. The prevailing investigations into RF EH-CRSNs primarily center around the resource allocation and protocol design issues, including clustering routing protocols [2], medium access control [3], and sensing and transmission strategies [4]. In these studies, CRSN nodes obtain energy and convey data solely via direct links with the RF source/data receiver. Severe propagation attenuation causes nodes located farther from the RF source to obtain less energy during downlink wireless energy delivery (DWED) and meanwhile need higher transmit power (TP) for uplink data reporting (UDR), which accelerates energy depletion and shortens the network operating time.

Intelligent reflecting surface (IRS) technology offers a new way to reconfigure the radio environment and has therefore been regarded as a promising means of improving wireless system performance [5]. IRS can generally be divided into passive IRS (PIRS) and active IRS (AIRS). By properly adjusting the phase shifts and/or amplitude of incident signals, a PIRS can create favourable signal superposition between the direct path and the reflected path, thereby enhancing the received signal strength and achieving a high beamforming gain. However, the performance gain of PIRS-aided transmission is fundamentally constrained by multiplicative fading effect, since the cascaded transmitter-PIRS-receiver link suffers the compounded path loss of its two constituent sub-links [6]. AIRS is introduced to alleviate this drawback by equipping each reflecting element (RE) with an active load, such as negative resistance [7], so that signal amplification can be incorporated together with phase regulation at the cost of additional but relatively low power consumption. The signal passing via the transmitter-AIRS-receiver link experiences path loss only in the AIRS-receiver

DOI: 10.13164/re.2026.0609

portion, effectively compensating for the multiplicative fading loss in the cascaded link [8]. Reference [9] suggests that AIRS outperforms PIRS in terms of performance gains, given an equal total power budget.

In AIRS-aided EH-CRSNs, all CRSN nodes first replenish their batteries with RF signals transmitted by the sink during the DWED phase, where a common reflection coefficient matrice (RCM) is employed by the AIRS. After that, the cluster heads (CHs) forward their sensed information to the sink during the UDR phase, and different RCMs can be configured for different CHs. There is no causal constraint imposed by the DWED on the UDR. Therefore, existing research on AIRS-aided wireless communication systems is not applicable to AIRS-aided EH-CRSNs. It is necessary to optimize the coordination between the uplink and downlink to achieve the dual goals of enhancing wireless energy delivery efficiency of CRSN nodes and reducing their energy consumption during UDR. In our previous study [10], we investigated AIRS-aided EH-CRSNs from the perspective of node-side energy sustainability. Specifically, the net energy gain (NEG), defined as the difference between the cumulative energy harvested by CRSN nodes during downlink wireless energy delivery and the energy consumed by CHs for uplink data reporting, was maximized through joint AIRS passive beamforming and deployment optimization. Since the sink was equipped with a single antenna and the uplink and downlink AIRS RCMs were independently involved in the corresponding transmission phases, the optimization problem at a given AIRS location could be decomposed into downlink harvested-energy maximization and uplink transmission-energy minimization. Nevertheless, maximizing node-side NEG does not necessarily lead to efficient energy utilization from a system perspective. In particular, a larger amplification capability of the AIRS can increase the harvested energy of CRSN nodes and reduce the transmission energy required by CHs, while simultaneously introducing additional circuit, biasing, signal-amplification, and noise-amplification energy expenditure at the AIRS. Therefore, an improvement in node-side NEG may be achieved at the expense of increased system-level energy consumption. This limitation is not merely associated with the choice of a different performance metric; rather, the node-centric energy-accounting boundary in [10] does not characterize the fundamental tradeoff between the communication gain provided by active reflection and the additional energy required for AIRS operation.

Motivated by this observation, this paper investigates a system-level energy efficiency (EE) design for AIRS-aided EH-CRSNs. Different from [10], a multi-antenna sink is considered, and the sink transmit beamformer for DWED, the sink receive beamformers for UDR, and the AIRS RCMs employed in the two phases are jointly designed. By incorporating the energy expenditure of the sink, CRSN nodes, and AIRS operation into a unified EE formulation, the sink beamforming variables and AIRS reflection coefficients become mutually coupled. Consequently, the uplink and downlink designs can no longer be independently optimized as in [11], leading to a fundamentally different optimization structure. The main contributions of this paper are summarized as follows.

1. A system-level EE optimization framework is formulated for AIRS-aided EH-CRSNs. To characterize the fundamental performance limits, this paper assumes that perfect channel state information (CSI) is known a priori. Furthermore, this paper also briefly analyzes the impact of varying degrees of channel errors on the performance limits. Unlike the node-side NEG formulation in [10], the proposed framework evaluates the information-delivery capability per unit of system energy expenditure and explicitly accounts for the additional energy required for AIRS operation. A multi-antenna sink is employed, and its downlink transmit beamformer and uplink receive beamformers are jointly designed with the AIRS RCMs under the sink transmit-power constraint and the AIRS amplification-power budget.

2. An iterative joint optimization framework is developed for the resulting coupled non-convex problem. The sink beamforming variables and AIRS reflection coefficients are partitioned into two variable blocks and updated alternately. Successive convex approximation (SCA) and semidefinite relaxation (SDR)-based techniques are then employed to handle the non-convex components arising in the corresponding subproblems. In contrast to [10], where the downlink and uplink designs can be optimized independently at a given AIRS location, the proposed framework addresses the mutual coupling between sink beamforming and AIRS reflection introduced by the system-level EE formulation.

3. Numerical results demonstrate the effectiveness of the proposed system-level design and reveal an energy-utilization tradeoff that cannot be characterized by the NEG-oriented formulation in [10]. In particular, increasing the AIRS APB or the number of active REs does not necessarily improve system EE. Beyond an appropriate operating region, the additional AIRS-side energy expenditure may outweigh the benefits obtained from enhanced DWED and reduced UDR energy, resulting in a decrease in overall EE. These results provide useful guidance for selecting AIRS operating parameters from a system-level EE perspective.

The remainder of this paper is organized as follows. Section 2 reviews the existing studies on AIRS- and PIRS-aided wireless communications. Section 3 presents the system model for AIRS-aided EH-CRSNs. Section 4 formulates a non-convex optimization problem to maximize the system EE of AIRS-aided EH-CRSNs and proposes a joint design to solve the formulated problem. Section 5 validates the effectiveness of the proposed joint design through numerical comparisons with benchmark schemes. Finally, Section 6 concludes the paper.

2. Related Work

This paper will now review the current research efforts in the areas of PIRS-aided and AIRS-aided wireless communication.

2.1 Research on PIRS-aided Wireless Communication

Researchers have investigated how the introduction of PIRS affects system performance in various scenarios, including mobile edge computing [11], terahertz communication [12], wireless energy transfer [13], and EH-CRSNs [14]. Specifically, [11] enhances the outage performance of mobile edge computing networks by deploying PIRS; reference [12] applies a delay module to each RE and addresses the beam misalignment issue caused by IRS by maximizing the weighted aggregate rate across all users; reference [13] incorporates PIRS into wireless energy transfer systems to improve the EH efficiency for all users. References [14] propose EH schemes for PIRS-aided EH-CRSNs. In [14], to achieve maximum cumulative energy harvested by all nodes, 3 methods are used to configure the PIRS RCM. Among them, the PIRS sub-surface partitioning-based method proves effective in boosting individual node harvesting efficiency while lower the problem-solving complexity. In response to the issue of uneven remaining energy among nodes caused by significant differences in EH levels in [14] formulates and solves an optimization problem aimed at optimizing the lowest EH level across overall nodes, maintaining energy equilibrium among all nodes by compromising the performance of some high-EH nodes. Nevertheless, the PIRS RCMs designed in [11], [12] to improve the data transmission efficiency are not applicable to the EH phase, failing to effectively address the energy constraints of battery-powered devices, which limits the system lifespan. Conversely, the PIRS RCMs configured in [13], [14] to enhance EH efficiency are not suitable for the data transmission phase, making it difficult to effectively reduce the energy expenditure of users/nodes in data transmission.

To improve both EH and data transmission efficiency, researchers have explored IRS-aided simultaneous wireless information and power transfer (SWIPT) [15–20] and IRS-aided wireless powered communication networks (WPCNs) [21–27]. SWIPT systems can be classified into 2 categories according to the type of receiving-end users: 1) The receiving-end users are of the same type, simultaneously receiving both information and energy signals, and employ time-switching or power-splitting receivers to decode information and harvest energy [15–17]. Specifically, [15], [16] place IRS on unmanned aerial vehicles (UAVs) and optimize the operation trajectory of UAVs by maximizing the weighted aggregate of all users' secrecy rates and minimizing the highest energy expenditure among all users, respectively. Reference [17] addresses the user aggregate rate maximization problem in IRS-aided SWIPT systems for massive machine-type communication scenarios and demonstrates that the proposed non-orthogonal multiple access (NOMA) transmission scheme can support simultaneous communication for a large amount of Internet of Things (IoT) devices with limited spectrum resources. 2) The receiving-end users include energy users who harvest energy and information users who transmit data [18–20]. Reference [18] investigates the optimization of weighted aggregate of power received by energy users, which significantly enhances wireless energy transfer efficiency and the rate-energy trade-off. Reference [19] examines the problem of minimizing the TP of the base station (BS), alleviating the operational burden on the BS and reducing system energy consumption. Reference [20] studies the problem of maximizing system EE while ensuring security and meeting EH requirements. In IRS-aided WPCNs, researchers have primarily explored maximizing the weighted aggregate rate of all users [21], robust resource allocation in secure communication scenarios [22], minimizing the system's total transmission time while considering IRS phase errors [23], and maximizing the average throughput of nodes by integrating IRS into UAVs [24]. Different from the above studies where the energy transmitter and signal receiver are the same BS, in [25–27], IRS-aided WPCNs adopt a dual-station configuration, with energy and signals radiated separately. These studies mainly focus on game theory-based energy trading and resource allocation between the power station and transmitter [25], system EE maximization [26], and maximizing the weighted sum throughput of all devices [27].

While PIRS can enhance wireless-system performance, the achievable gain is fundamentally limited by the multiplicative-fading effect in the cascaded channel. In addition, obtaining strong beamforming gains usually requires a large number of passive REs, which reduces the suitability of PIRS for space-constrained deployments. The use of many REs also increases the burden of channel estimation and complicates the associated optimization design, thereby limiting practical implementation.

2.2 Research on AIRS-aided Wireless Communication

To further enhance system performance, researchers have conducted a series of studies on AIRS-aided wireless communication systems. Reference [28] evaluates the performance of AIRS-aided NOMA networks in terms of user outage probability and system throughput. In the context of physical layer security, the problem of maximizing the secrecy rate in secure communication systems [29] and the problem of maximizing the convert rate in convert communication systems [30] are studied, respectively. Reference [31] investigated the EE maximization problem for AIRS-aided uplink NOMA systems. However, the aforementioned systems typically rely on traditional battery-powered devices, and the lack of additional energy supplementation may compromise the system's long-term operational capability. To overcome the network's energy limitations and achieve green communication, [32–35] combine AIRS with RF EH technology, exploring AIRS-aided WPCNs [32], [33], and SWIPT systems [36], [37]. Specifically, [32] is the first to apply AIRS

Reference	Year	Application scenarios	EH	Consideration of energy consumption	Use of AIRS	Joint uplink-downlink optimization	Optimization objectives
[10]	2024	EH-CRSNs	✓	✓	✓	✓	Max NEG
[13]	2023	EH WET	✓	×	✓	×	Max EH
[14]	2022	EH-CRSNs	✓	×	×	×	Max EH
[15]	2024	UAV SWIPT	✓	✓	×	×	Max secrecy rate
[16]	2023	UAV SWIPT	✓	✓	×	×	Max sum rate
[17]	2023	FD NOMA	✓	×	×	✓	Max sum rate
[18]	2020	MISO SWIPT	✓	×	×	×	Max weighted sum-power
[19]	2022	NOMA SWIPT	✓	×	×	×	Min TP
[20]	2023	MISO SWIPT	✓	✓	×	×	Max EE
[21]	2023	UAV WPCNs	✓	✓	×	✓	Max sum rate
[22]	2023	MISO WPCNs	✓	✓	×	✓	Min TP
[23]	2023	FD-WPCNs	✓	✓	×	✓	Min transmission time
[24]	2024	UAV WPCNs	✓	×	×	✓	Max throughput
[25]	2023	MISO WCSs	✓	×	×	✓	Max utility function
[26]	2022	WPT IIOT	✓	✓	×	✓	Max EE
[27]	2024	FD-WPCNs	✓	✓	×	×	Max sum rate
[28]	2023	NOMA WCSs	×	×	✓	×	Max SINR
[29]	2022	MISO WCSs	×	×	✓	×	Max secrecy rate
[30]	2023	SISO WCSs	×	×	✓	×	Max SNR
[31]	2024	NOMA WCSs	×	✓	✓	×	Max EE
[32]	2022	SISO WPCNs	✓	✓	✓	✓	Max throughput
[33]	2024	SISO WPCNs	✓	✓	✓	✓	Max throughput
[34]	2023	MISO SWIPT	✓	×	✓	×	Max weighted sum-power
[35]	2024	MISO SWIPT	✓	×	✓	×	Max power harvested
Ours	–	EH-CRSNs	✓	✓	✓	✓	Max EE

Note: WET represents wireless energy transfer. FD represents full-duplex. MISO denotes multiple-input single-output. WPT is the abbreviation for wireless power transfer. IIOT represents industrial IoT. WCSs denotes wireless communication systems. SISO means single-input single-output. SINR represents signal to interference plus noise ratio. SNR represents signal-to-noise ratio.

Tab. 1. Comparative analysis of existing literature.

in WPCNs and investigates the optimization of weighted aggregate throughput across all devices under 3 different IRS beamforming configurations, demonstrating that AIRS can achieve higher throughput while reducing system energy consumption. Reference [33] focuses on maximizing the total system throughput using NOMA technology, showing that AIRS has the potential to improve the throughput and coverage of WPCNs. Reference [34] studies the joint beamforming optimization problem of the wireless access point and AIRS with the goals of maximizing the weighted aggregate of the received power of energy users and the weighted aggregate rate of information users, highlighting the advantages of AIRS in enhancing overall system performance. Reference [35] addresses the problem of maximizing the received power of EH receivers under both perfect and imperfect CSI conditions, confirming the effectiveness of the 2 proposed beamforming schemes. Table 1 summarizes the differences between the existing literature and the present study, with "✓" and "×" marking whether a specific feature is considered. It is worth further distinguishing the present study from our previous AIRS-aided EH-CRSN work [10]. Although both studies consider downlink EH and UDR, their design scopes are different. Reference [10] adopts a single-antenna sink and focuses on maximizing node-side NEG by optimizing the AIRS RCMs and deployment location. At a fixed AIRS location, its downlink harvested-energy maximization and uplink transmission-energy minimization problems are separable and can be solved independently. In contrast, this work employs a multi-antenna sink and investigates system-level EE by jointly optimizing the sink transmit/receive beamformers and the AIRS RCMs. Moreover, the energy expenditure associated with AIRS operation is incorporated into the system-level energy accounting. These extensions introduce mutual coupling between the sink beamforming variables and AIRS reflection coefficients and lead to an optimization structure fundamentally different from that in [10]. In AIRS-aided WPCNs, users convert the energy signals received from the RF source through the downlink into electrical energy and utilize the harvested energy for UDR, where the DWED imposes an energy causality constraint on the UDR. Conversely, in AIRS-aided EH-CRSNs, the downlink energy gathered by nodes only aids in charging the nodes' battery and does not impose any causality constraint. In an AIRS-aided SWIPT system, the BS simultaneously transmits data and energy through the downlink, necessitating careful design to strike a balance between EH and data transmission. In contrast, in AIRS-aided EH-CRSNs, all CRSN nodes first obtain RF energy via the downlink and then perform data reporting via the uplink. Therefore, it is essential to coordinate and optimize the uplink and downlink to simultaneously achieve the dual goals of enhancing wireless energy delivery efficiency and reducing the energy expenditure of UDR. These differences, together with the limitations of the node-centric NEG design in [10], motivate us to investigate a system-level EE

framework that jointly coordinates multi-antenna sink beamforming and AIRS reflection design for both DWED and UDR.

3. System Model

In this paper, we investigate the AIRS-assisted EH-CRSN system shown in Fig. 1. In the considered AIRS-aided EH-CRSN, the sink employs N_{t} antenna elements for DWED and data reception. The AIRS is composed of M REs, Meanwhile, N CRSN nodes are scattered throughout disk-shaped sensing area of size A, where each node adopts a single-antenna configuration. They are arranged into K clusters following a conventional clustering algorithm [36]. For geometric description, a 3D Cartesian coordinate representation is employed. The sink and the CRSN nodes are placed on the ground plane. Specifically, the sink is set at the origin $(0,0,0)$ and CRSN node $n(\forall n \in \{1,\ldots,N\})$ at $(x_n, y_n, 0)$. The AIRS is installed horizontally with respect to the ground plane, and its altitude is set to H_{IRS}. It is capable of moving in the direction parallel to the y-axis, and its center is given by $(0, y_{\mathrm{IRS}}, H_{\mathrm{IRS}})$. By appropriately configuring the RCM $\mathbf{\Phi} = \mathrm{diag}(\phi_1,\ldots,\phi_m,\ldots,\phi_M) \in \mathrm{C}^{M\times M}$, the transmitted signal strength between the sink and the CRSN nodes can be enhanced. For the m^{th} RE, $\phi_m = a_m \exp(\mathrm{j}\theta_m)$ denotes its reflection coefficient, where $a_m \geq 1$ and $\theta_m \in [0, 2\pi)$ represent the reflection amplitude and phase shift, respectively. The equivalent baseband channels for the AIRS-sink link, CRSN node n-AIRS link, and CRSN node n-sink link are represented as $\mathbf{g} \in \mathrm{C}^{N_{\mathrm{t}}\times M}$, $\mathbf{h}_{r,n} \in \mathrm{C}^{M\times 1}$, and $\mathbf{h}_{d,n} \in \mathrm{C}^{N_{\mathrm{t}}\times 1}$, respectively, for all $n \in \{1,\ldots,N\}$. In addition, the instantaneous CSI of all channels is assumed to be available through existing IRS-aided channel-estimation approaches, such as compressive sensing [37] or data augmentation-based data-driven methods [38]. However, in practical implementations, the absence of RF chains makes it challenging for AIRS-aided EH-CRSNs to acquire perfectly accurate CSI. Accordingly, the channel coefficients used in the optimization framework are regarded as the estimated CSI available to the system. To evaluate the impact of imperfect CSI, the actual channel is modeled as the sum of the estimated channel and a channel estimation error. The optimization variables are first obtained based on the estimated CSI and are subsequently applied to the actual channels. Therefore, channel estimation errors result in a mismatch between the optimization solution obtained from the estimated CSI and the actual propagation conditions, which may degrade the energy-transfer and information-transmission performance. The resulting effects on the system energy consumption and EE are quantitatively evaluated in Sec. 5. Additionally, we assume that all CRSN nodes operate in a time-division duplexing (TDD) mode, wherein each node alternates between data reporting and wireless energy reception across distinct time slots, with the uplink and downlink sharing the same frequency band. On this basis, channel reciprocity is further assumed, meaning that the uplink and downlink channel gains remain symmetric within the channel coherence time.

As depicted in Fig. 2 at the top of the next page, each operating round of the AIRS-aided EH-CRSN can be divided into 2 phases: 1) In the DWED phase with duration τ_0, the sink radiates RF energy signals to charge the batteries of all CRSN nodes; 2) In the subsequent UDR phase lasting $T - \tau_0$, the cluster members (CMs) of the k^{th} cluster $(\forall k \in \{1,\ldots,K\})$ report data collected from the surrounding environment to CH k in a time-division manner within τ_{intra}. CH k then receives the data and forwards the compressed and aggregated data within $\tau_k = (T - \tau_0 - \tau_{\mathrm{intra}})/K$.

Specifically, during the DWED phase, each CRSN node obtains energy from both the direct sink-to-node link and the AIRS-aided cascaded link. The received RF signal is converted into electricity with conversion efficiency $\eta(\eta \in (0,1])$. The overall energy gathered within the τ_0 time period is:

$$E_{\mathrm{har}} = \tau_0 \eta \sum_{n=1}^{N} \left(P_{\mathrm{S}} |(\mathbf{h}_{d,n}^{\mathrm{H}} + \mathbf{h}_{r,n}^{\mathrm{H}} \mathbf{\Phi}_0 \mathbf{g}^{\mathrm{H}}) \boldsymbol{\omega}_0|^2 + \sigma_1^2 || \mathbf{h}_{r,n}^{\mathrm{H}} \mathbf{\Phi}_0 ||^2 + \sigma_{3,n}^2 \right) \tag{1}$$

where P_{S} denotes the maximum TP of the sink. $\mathbf{\Phi}_0 = \mathrm{diag}(\phi_{0,1},\ldots,\phi_{0,m},\ldots,\phi_{0,M})$ denotes the AIRS RCM during the DWED phase. $\boldsymbol{\omega}_0 = [\omega_{0,1},\ldots,\omega_{0,N_{\mathrm{t}}}]^{\mathrm{T}} \in \mathrm{C}^{N_{\mathrm{t}}\times 1}$ is the sink transmit beamformer. σ_1^2 and $\sigma_{3,n}^2$ stand for the receiver noise terms of the AIRS and CRSN node n, respectively.

During the DWED phase, the system's energy consumption is given by (2):

$$E_{\mathrm{DLcon}} = \tau_0 (P_{\mathrm{S}} ||\boldsymbol{\omega}_0||^2 + M \times P_{\mathrm{irs}} + P_{\mathrm{S}} ||\mathbf{\Phi}_0 \mathbf{g}^{\mathrm{H}} \boldsymbol{\omega}_0||^2 + \sigma_1^2 ||\mathbf{\Phi}_0 \mathbf{I}_M||^2) \tag{2}$$

where $P_{\mathrm{S}}||\boldsymbol{\omega}_0||^2$ is the actual TP of the sink. P_{irs} is composed of the circuit energy consumption P_{C} and DC biasing energy consumption P_{DC} of each active RE. $P_{\mathrm{S}}||\mathbf{\Phi}_0 \mathbf{g}^{\mathrm{H}} \boldsymbol{\omega}_0||^2$ and $\sigma_1^2 ||\mathbf{\Phi}_0 \mathbf{I}_M||^2$ denote the signal power amplified by the AIRS and the dynamic noise power, respectively.

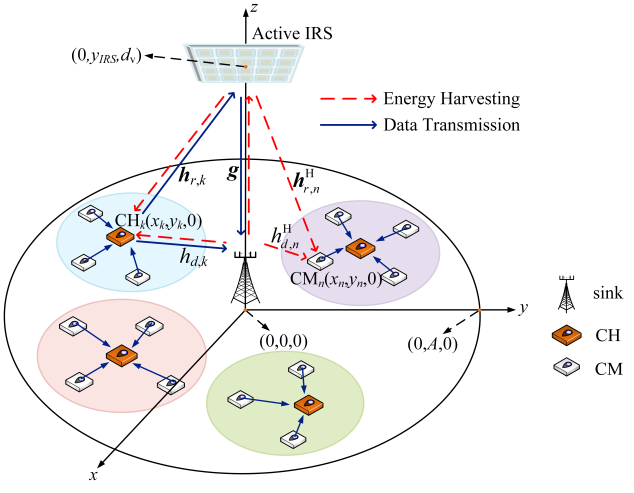


Fig. 1. System model of AIRS-assisted EH-CRSNs.

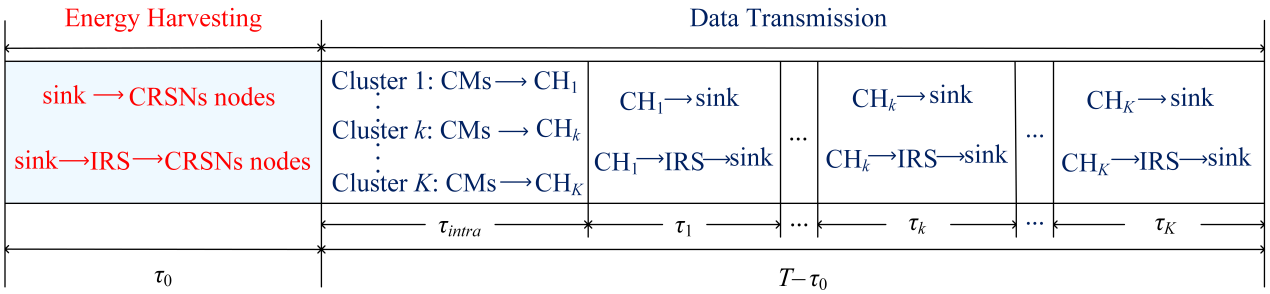


Fig. 2. Transmission frame structure for AIRS-aided EH-CRSNs.

During the UDR phase, K clusters perform intra-cluster time-division data reporting in parallel within the time period τ_{intra}. Since the received signal-to-noise ratio (SNR) threshold at all CHs is fixed at $SNR_{\text{threshold}}$, the corresponding reporting rate per cluster is $R_{\text{intra}} = B\log_2(1+SNR_{\text{threshold}})$, where B is the channel bandwidth. Because of the complexity of intra-cluster AIRS-aided communication and the significantly limited capability to reduce energy consumption for intra-cluster communication, this paper only employs the AIRS to assist CHs in reporting data to the sink. The SNR at the sink when receiving uplink data from CH k is:

$$SNR_k = \frac{p_k\left|\boldsymbol{\omega}_k^{\mathrm{H}}(\mathbf{h}_{d,k}+\mathbf{g}\boldsymbol{\Phi}_k\mathbf{h}_{r,k})\right|^2}{\sigma_1^2\left|\left|\boldsymbol{\omega}_k^{\mathrm{H}}\mathbf{g}\boldsymbol{\Phi}_k\right|\right|^2+\sigma_2^2||\boldsymbol{\omega}_k||^2} \tag{3}$$

where $\boldsymbol{\omega}_k = [\omega_{k,1},\ldots,\omega_{k,N_t}]^{\mathrm{H}} \in \mathrm{C}^{N_t\times 1}$ represents the sink receive beamformer during time slot τ_k. σ_2^2 indicates the receiver noise terms of the sink. $\boldsymbol{\Phi}_k = \mathrm{diag}(\phi_{k,1},\ldots,\phi_{k,m},\ldots,\phi_{k,M})$ indicates the AIRS RCM assisting CH k for UDR, and $\phi_{k,m} = a_{k,m}\exp(\mathrm{j}\theta_{k,m})(\forall k \in \{1,\ldots,K\}, \forall m \in \{1,\ldots,M\})$. p_k is the TP of CH k. When the received SNR threshold is set to $SNR_{\text{threshold}}$, the expression for p_k is:

$$p_k = \frac{\sigma_1^2\left|\left|\boldsymbol{\omega}_k^{\mathrm{H}}\mathbf{g}\boldsymbol{\Phi}_k\right|\right|^2+\sigma_2^2||\boldsymbol{\omega}_k||^2}{\left|\boldsymbol{\omega}_k^{\mathrm{H}}(\mathbf{h}_{d,k}+\mathbf{g}\boldsymbol{\Phi}_k\mathbf{h}_{r,k})\right|^2}\times SNR_{\text{threshold}}. \tag{4}$$

The UDR rate of CH k is:

$$R_k = B\log_2(1+SNR_{\text{threshold}}). \tag{5}$$

The energy expenditure of the system during the UDR phase is given by (6) at the bottom of this page.

Here, $p_k||\boldsymbol{\Phi}_k\mathbf{h}_{r,k}||^2$ and $\sigma_1^2||\boldsymbol{\Phi}_k\mathbf{I}_M||^2$ refer to the power of the incident signal from CH k amplified by the AIRS and the dynamic noise power, respectively. The energy expenditure of the sink for receiving data transmitted by CHs is given by $E_{\text{sink}} = K\times E_{\text{elec}}\times L$. Here, E_{elec} represents the electronic circuitry energy consumption per unit of data transmission/reception, and L is the data packet size. The average energy expenditure of CH k for receiving and aggregating data from its CMs is represented as $E_{\text{CHintra}} = (N/K-1)(E_{\text{elec}}+E_{\text{DA}})\times L$. Here, $N/K-1$ is the average count of CMs in the cluster of CH k, and E_{DA} is the energy consumption for data aggregation per unit of data. $N-K$ is the count of CMs in the monitoring area. E_{CM} denotes the energy expenditure of a CM for reporting data to its CH, which can be quantified using the free-space or multi-path fading loss models according to the transmitter-receiver distance d and the threshold d_0, as detailed in (7). ε_{fs} and ε_{mp} represent the energy expenditure coefficients of the power amplifier circuits under the free-space and two-ray ground reflection path loss models, respectively. When $d \le d_0 = \sqrt{\varepsilon_{\text{fs}}/\varepsilon_{\text{mp}}}$, the transmission loss exhibits a proportional relationship to d^2. Otherwise, it is proportional to d^4 [39].

$$E_{\text{CM}} = \begin{cases} L\times(E_{\text{elec}}+\varepsilon_{\text{fs}}d^2) & \text{if} \quad d\le d_0 \\ L\times(E_{\text{elec}}+\varepsilon_{\text{mp}}d^4) & \text{else} \end{cases}. \tag{7}$$

4. Problem Formulation and Solving

For the considered AIRS-aided EH-CRSN, the objective is to maximize the system EE by jointly optimizing the sink transmit beamformer for DWED, the sink receive beamformers for UDR, and the AIRS RCMs employed in the two phases. Since the energy harvested by CRSN nodes replenishes the node batteries, the net system energy expenditure over one operating round is characterized by the difference between the total consumed energy and the harvested energy. Based on the CSI assumption described in Sec. 3, the optimization problem is formulated as follows using the estimated CSI available to the system. The impact of the mismatch between the estimated and actual CSI on the resulting optimization solution is further evaluated in Sec. 5.

$$E_{\text{ULcon}} = \sum_{k=1}^{K}(\tau_k\times(p_k+p_k||\boldsymbol{\Phi}_k\mathbf{h}_{r,k}||^2+\sigma_1^2||\boldsymbol{\Phi}_k\mathbf{I}_M||^2+M\times P_{\text{irs}})+(E_{\text{elec}}+E_{\text{DA}})\times L)+E_{\text{sink}}+(N-K)\times E_{\text{CM}} + K\times E_{\text{CHintra}}. \tag{6}$$

$$\mathbf{P1} \max_{\boldsymbol{\omega}_0,\{\boldsymbol{\omega}_k\},\boldsymbol{\Phi}_0,\{\boldsymbol{\Phi}_k\}} \quad EE = \frac{R_{\text{total}}}{E_{\text{sys}}} = \frac{R_{\text{total}}}{E_{\text{ULcon}} + E_{\text{DLcon}} - E_{\text{har}}} \tag{8a}$$

$$\text{s.t.} \frac{\sigma_1^2 ||\boldsymbol{\omega}_k^{\text{H}} \mathbf{g} \boldsymbol{\Phi}_k||^2 + \sigma_2^2 ||\boldsymbol{\omega}_k||^2}{|\boldsymbol{\omega}_k^{\text{H}} (\mathbf{h}_{d,k} + \mathbf{g} \boldsymbol{\Phi}_k \mathbf{h}_{r,k})|^2} \times SNR_{\text{threshold}} \times ||\boldsymbol{\Phi}_k \mathbf{h}_{r,k}||^2 + \sigma_1^2 ||\boldsymbol{\Phi}_k \mathbf{I}_M||^2 \leq P_{\text{out}}, \forall k \in \{1, \ldots, K\}, \tag{8b}$$

$$P_{\text{S}} ||\boldsymbol{\Phi}_0 \mathbf{g}^{\text{H}} \boldsymbol{\omega}_0||^2 + \sigma_1^2 ||\boldsymbol{\Phi}_0 \mathbf{I}_M||^2 \leq P_{\text{out}}, \tag{8c}$$

$$||\boldsymbol{\omega}_k||^2 \leq 1, \quad \forall k \in \{1, \ldots, K\}, \tag{8d}$$

$$||\boldsymbol{\omega}_0||^2 \leq 1, \tag{8e}$$

$$|\phi_{k,m}|^2 \geq 1, \quad \forall k \in \{1, \ldots, K\}, \forall m \in \{1, \ldots, M\}, \tag{8f}$$

$$|\phi_{0,m}|^2 \geq 1, \quad \forall m \in \{1, \ldots, M\} \tag{8g}$$

where $R_{\text{total}} = (R_{\text{intra}} \times K \times \tau_{\text{intra}} + \sum_{k=1}^{K} \tau_k \times R_k)/(T - \tau_0)$ denotes the overall achievable information rate during the UDR phase. $R_{\text{intra}} \times K \times \tau_{\text{intra}}$ represents the volume of reported data during intra-cluster communication in the UDR phase while $\sum_{k=1}^{K} \tau_k \times R_k$ corresponds to the data forwarded from the CHs to the sink. The terms E_{ULcon}, E_{DLcon}, and E_{har}, defined in (6), (2), and (1), respectively, denote the system energy expenditure during UDR, the system energy expenditure during DWED, and the energy harvested by all CRSN nodes during DWED. The considered operating regime satisfies $E_{\text{ULcon}} + E_{\text{DLcon}} > E_{\text{har}}$, such that the denominator of the EE metric remains positive. The design variables $\boldsymbol{\omega}_0$ and $\boldsymbol{\omega}_k$ denote the sink transmit and receive beamformers, respectively, whereas $\boldsymbol{\Phi}_0$ and $\boldsymbol{\Phi}_k$ denote the AIRS RCMs employed during DWED and the kth UDR time slot, respectively. Constraints (8b) and (8c) limit the AIRS amplification power in the UDR phase and the DWED phase, respectively. P_{out} denotes the maximum amplification power that the AIRS can supply. Equations (8d) and (8e) impose the constraints on the sink receive beamformer in the k^{th} UDR slot and the sink transmit beamformer in the DWED phase, respectively. Equation (8f) represents the reflection coefficient constraint for the AIRS during the k^{th} time slot of the UDR phase, and (8g) represents the reflection coefficient constraint for the AIRS during the DWED phase.

Problem (**P1**) is non-convex because both the objective function and several constraints involve strongly coupled optimization variables, which makes direct global optimization intractable. To address this difficulty, this paper divides all variables into 2 groups: 1) the sink transmit and receive beamformers $\{\boldsymbol{\omega}_0, \boldsymbol{\omega}_k\}$; 2) the AIRS RCMs $\{\boldsymbol{\Phi}_0, \boldsymbol{\Phi}_k\}$ used in the DWED and UDR phases. An alternating optimization (AO) framework is then employed to update these 2 groups iteratively until convergence occurs.

4.1 Optimizing the AIRS RCMs

Given the fixed sink transmit beamformer $\boldsymbol{\omega}_0$ and receive beamformer $\boldsymbol{\omega}_k$, the optimization problem for the AIRS RCMs $\{\boldsymbol{\Phi}_0, \boldsymbol{\Phi}_k\}$ is formulated as follows:

$$\mathbf{P2} \max_{\{\boldsymbol{\Phi}_k\},\boldsymbol{\Phi}_0} \frac{(R_{\text{intra}} \times K \times \tau_{\text{intra}} + \sum_{k=1}^{K} \tau_k \times R_k)/(T - \tau_0)}{E_{\text{ULcon}} + E_{\text{DLcon}} - E_{\text{har}}} \tag{9a}$$

$$\text{s.t.} \quad (8\text{b}), (8\text{c}), (8\text{f}), (8\text{g}). \tag{9b}$$

Let $\boldsymbol{\theta}_k = [\theta_{k,1}, \ldots, \theta_{k,m}, \ldots, \theta_{k,M}]^{\text{T}}$. During the UDR phase, all CHs upload their data to the sink over orthogonal time slots. To ensure phase coherence between the signals conveyed via both the cascaded and direct links, the optimal reflection phase shift of the $m^{\text{th}} (\forall m \in \{1, \ldots, M\})$ active RE for assisting CH k in UDR, as specified in [9], is:

$$\theta_{k,m} = \text{mod}\ [\arg(\bar{h}_{d,k}) - \arg([h_{r,k}]_m) - \arg(\bar{g}_m), 2\pi] \tag{10}$$

where arg $\{\cdot\}$ indicates the phase of the signal. $\bar{h}_{d,k} = \boldsymbol{\omega}_k^{\text{H}} \mathbf{h}_{d,k}$ and $\bar{\mathbf{g}} = \boldsymbol{\omega}_k^{\text{H}} \mathbf{g}$.

Let $\mathbf{a}_k = [a_{k,1}, \ldots, a_{k,m}, \ldots, a_{k,M}]^{\text{T}}$, $\mathbf{v}_0 = [\phi_{0,1}, \ldots, \phi_{0,m}, \ldots, \phi_{0,M}]^{\text{H}}$, $\bar{h}_{d,n}^{\text{H}} = \mathbf{h}_{d,n}^{\text{H}} \boldsymbol{\omega}_0$, $\mathbf{b}_k^{\text{H}} = \bar{\mathbf{g}} \text{diag}(\mathbf{h}_{r,k})$, $\mathbf{G} = \text{diag}([|\bar{g}_1|^2, \ldots, |\bar{g}_M|^2])$,

$$\mathbf{P3} \min_{\{\mathbf{a}_k\},\mathbf{v}_0} \sum_{k=1}^{K} (\tau_k \times (\frac{\sigma_1^2 \mathbf{a}_k^{\text{T}} \mathbf{G} \mathbf{a}_k + \sigma_2^2 \bar{\omega}_k}{||\bar{h}_{d,k}| + \bar{\mathbf{b}}_k^{\text{T}} \mathbf{a}_k|^2} \times SNR_{\text{threshold}} + \frac{\sigma_1^2 \mathbf{a}_k^{\text{T}} \mathbf{G} \mathbf{a}_k + \sigma_2^2 \bar{\omega}_k}{||\bar{h}_{d,k}| + \bar{\mathbf{b}}_k^{\text{T}} \mathbf{a}_k|^2} \times SNR_{\text{threshold}} \times \mathbf{a}_k^{\text{T}} \mathbf{H}_{r,k} \mathbf{a}_k + \sigma_1^2 \mathbf{a}_k^{\text{T}} \mathbf{I}_M \mathbf{a}_k$$

$$+M \times P_{\text{irs}}) + (E_{\text{elec}} + E_{\text{DA}}) \times L) + E_{\text{dt}} + E_{\text{eh}} + \tau_0 \times \mathbf{v}_0^{\text{H}} \mathbf{G}_0 \mathbf{v}_0 - \tau_0 \eta \sum_{n=1}^{N} (P_{\text{S}} \left|\bar{h}_{d,n} + \mathbf{b}_n^{\text{H}} \mathbf{v}_0\right|^2 + \sigma_1^2 \mathbf{v}_0^{\text{H}} \mathbf{H}_{r,n} \mathbf{v}_0 + \sigma_{3,n}^2) \tag{11a}$$

$$\text{s.t.} \quad \frac{\sigma_1^2 \mathbf{a}_k^{\text{T}} \mathbf{G} \mathbf{a}_k + \sigma_2^2 \bar{\omega}_k}{||\bar{h}_{d,k}| + \bar{\mathbf{b}}_k^{\text{T}} \mathbf{a}_k|^2} \times SNR_{\text{threshold}} \times \mathbf{a}_k^{\text{T}} \mathbf{H}_{r,k} \mathbf{a}_k + \sigma_1^2 \mathbf{a}_k^{\text{T}} \mathbf{I}_M \mathbf{a}_k \leq P_{\text{out}}, \ \forall k \in \{1, \ldots, K\}, \tag{11b}$$

$$\mathbf{v}_0^{\text{H}} \mathbf{G}_0 \mathbf{v}_0 \leq P_{\text{out}}, \tag{11c}$$

$$a_{k,m} \geq 1, \quad \forall k \in \{1, \ldots, K\}, \ \forall m \in \{1, \ldots, M\}, \tag{11d}$$

$$\left|v_{0,m}\right|^2 \geq 1, \quad \forall m \in \{1, \ldots, M\}. \tag{11e}$$

$\bar{\mathbf{g}}_0^{\mathrm{H}} = \mathbf{g}^{\mathrm{H}}\boldsymbol{\omega}_0$, $\mathbf{b}_n^{\mathrm{H}} = \bar{\mathbf{g}}_0\mathrm{diag}(\mathbf{h}_{r,n})$, $\mathbf{G}_0 = P_{\mathrm{S}}\mathrm{diag}(|[\bar{g}_0]_1|^2,\ldots,|[\bar{g}_0]_M|^2) + \sigma_1^2\mathbf{I}_M$, $\bar{\omega}_0 = ||\boldsymbol{\omega}_0||^2$, $\bar{\omega}_k = ||\boldsymbol{\omega}_k||^2$, $\mathbf{H}_{r,k} = \mathrm{diag}(|[h_{r,k}]_1|^2,\ldots,\left|[h_{r,k}]_M\right|^2)$, and $\mathbf{H}_{r,n} = \mathrm{diag}(\left|[h_{r,n}]_1\right|^2,\ldots,\left|[h_{r,n}]_M\right|^2)$. When the received SNR threshold $SNR_{\mathrm{threshold}}$ is fixed during the UDR phase, the numerator of the objective function (9a) becomes a constant term and is independent of the optimization variables $\{\mathbf{a}_k, \mathbf{v}_0\}$. Thus, maximizing EE can be transformed into minimizing E_{total}. By applying the optimal reflection phase shift $\theta_{k,m}$ as shown in (10), problem (**P2**) is alternatively expressed as (11) at the bottom of the previous page. Here, $\bar{\mathbf{b}}_k^{\mathrm{T}} = |\mathbf{b}_k^{\mathrm{H}}|$, $v_{0,m} = \phi_{0,m}$, $E_{\mathrm{dt}} = E_{\mathrm{sink}} + (N-K)\times E_{\mathrm{CM}} + K\times E_{\mathrm{CHintra}}$, and $E_{\mathrm{eh}} = \tau_0\times(P_{\mathrm{S}}\bar{\omega}_0 + M\times P_{\mathrm{irs}})$.

Although this reformulation simplifies the structure of the objective, problem (**P3**) is still non-convex due to the coupled quadratic and fractional terms appearing in both the objective function and the constraints. According to [7], this paper uses the SCA technique to solve this optimization problem. Specifically, let $\boldsymbol{\Xi} = P_{\mathrm{S}}\sum_{n=1}^{N}\mathbf{b}_n\mathbf{b}_n^{\mathrm{H}}$ and $\boldsymbol{\Pi} = \sigma_1^2\sum_{n=1}^{N}\mathbf{H}_{r,n}$ the non-convex terms are replaced by their first-order lower-bound approximations around feasible operating points, yielding the approximations in (12)–(14).

$$\mathbf{v}_0^{\mathrm{H}}\boldsymbol{\Xi}\mathbf{v}_0 \geq 2\,\mathrm{Re}\{\mathbf{v}_0^{\mathrm{H}}\boldsymbol{\Xi}\mathbf{v}_0^{q-1}\} - \left(\mathbf{v}_0^{q-1}\right)^{\mathrm{H}}\boldsymbol{\Xi}\mathbf{v}_0^{q-1}, \tag{12}$$

$$2\,\mathrm{Re}\{\mathbf{v}_0^{\mathrm{H}}(\boldsymbol{\Xi}\mathbf{v}_0^{q-1} + P_{\mathrm{S}}\sum_{n=1}^{N}\mathbf{b}_n\bar{h}_{d,n} + \boldsymbol{\Pi}\mathbf{v}_0^{q-1})\} - \left(\mathbf{v}_0^{q-1}\right)^{\mathrm{H}}\boldsymbol{\Xi}\mathbf{v}_0^{q-1} - \left(\mathbf{v}_0^{q-1}\right)^{\mathrm{H}}\boldsymbol{\Pi}\mathbf{v}_0^{q-1} + P_{\mathrm{S}}\sum_{n=1}^{N}\left|\bar{h}_{d,n}\right|^2 + \sum_{n=1}^{N}\sigma_{3,n}^2 \triangleq f(\mathbf{v}_0, \mathbf{v}_0^{q-1}), \tag{13}$$

$$\left|v_{0,m}\right|^2 \geq 2\mathrm{Re}\{(v_{0,m})^* v_{0,m}^{q-1}\} - \left|v_{0,m}^{q-1}\right|^2 \tag{14}$$

where $v_{0,m}^{q-1}$ is the feasible point, and $(v_{0,m})^*$ represents the conjugate of $v_{0,m}$.

To handle the remaining coupled fractional terms in (**P3**), we introduce two nonnegative auxiliary variables t_k and u_k for each CH k. Let $q_k(\mathbf{a}_k) = \left\||\bar{h}_{d,k}| + \bar{\mathbf{b}}_k^{\mathrm{T}}\mathbf{a}_k\right\|^2$, since t_k and u_k appear in the objective with positive coefficients, the corresponding inequalities are active at the optimum. Therefore, after omitting the constant terms independent of the optimization variables, (**P3**) can be equivalently reformulated as:

$$\mathbf{P4}: \min_{\{\mathbf{a}_k,t_k,u_k\},\mathbf{v}_0} \sum_{k=1}^{K}(\tau_k\times(t_k\times SNR_{\mathrm{threshold}} + SNR_{\mathrm{threshold}}\times u_k + \sigma_1^2\mathbf{a}_k^{\mathrm{T}}\mathbf{I}_M\mathbf{a}_k + M\times P_{\mathrm{irs}})) + \tau_0\times\mathbf{v}_0^{\mathrm{H}}\mathbf{G}_0\mathbf{v}_0 - \tau_0\eta\times f(\mathbf{v}_0,\mathbf{v}_0^{q-1}) \tag{15a}$$

$$\text{s.t.}\quad SNR_{\mathrm{threshold}}\times u_k + \sigma_1^2\mathbf{a}_k^{\mathrm{T}}\mathbf{I}_M\mathbf{a}_k \leq P_{\mathrm{out}}, \quad \forall k\in\{1,\ldots,K\}, \tag{15b}$$

$$t_k\mathbf{a}_k^{\mathrm{T}}\mathbf{H}_{r,k}\mathbf{a}_k \leq u_k, \quad \forall k\in\{1,\ldots,K\}, \tag{15c}$$

$$\frac{\sigma_1^2\mathbf{a}_k^{\mathrm{T}}\mathbf{G}\mathbf{a}_k + \sigma_2^2\bar{\omega}_k}{t_k} \leq q_k(\mathbf{a}_k), \quad \forall k\in\{1,\ldots,K\} \tag{15d}$$

$$2\mathrm{Re}\{(v_{0,m})^* v_{0,m}^{q-1}\} - \left|v_{0,m}^{q-1}\right|^2 \geq 1, \quad \forall m\in\{1,\ldots,M\}, \tag{15e}$$

$$(11\mathrm{c}),\ (11\mathrm{d}) \tag{15f}$$

where (15c)–(15d) are the upper-bound constraints resulting from introducing the auxiliary variables t_k and u_k, and (15e) is obtained by jointly transforming (11e) and (14).

Although (15d) has a convex quadratic-over-linear term on its left-hand side, its right-hand side is convex, and thus the resulting constraint is still non-convex. Moreover, (15c) contains a product between t_k and a quadratic function of $\mathbf{a}_k$. To construct a valid inner convex approximation, the two constraints are treated separately as follows.

For (15d), because $q_k(\mathbf{a}_k)$ is convex, its first-order Taylor expansion at the feasible point $\mathbf{a}_k^{(q-1)}$ provides a global affine lower bound:

$$q_k(\mathbf{a}_k) \geq \underline{q}_k^{(q)}(\mathbf{a}_k) \tag{16}$$

where

$$\underline{q}_k^{(q)}(\mathbf{a}_k) = q_k(\mathbf{a}_k^{(q-1)}) + 2\left(|\bar{h}_{d,k}| + \bar{\mathbf{b}}_k^{\mathrm{T}}\mathbf{a}_k^{(q-1)}\right)\bar{\mathbf{b}}_k^{\mathrm{T}}\left(\mathbf{a}_k - \mathbf{a}_k^{(q-1)}\right). \tag{17}$$

Accordingly, the following conservative inner approximation of (15d) is adopted:

$$\frac{\sigma_1^2\mathbf{a}_k^{\mathrm{T}}\mathbf{G}\mathbf{a}_k + \sigma_2^2\bar{\omega}_k}{t_k} \leq \underline{q}_k^{(q)}(\mathbf{a}_k), \quad \forall k\in\{1,\ldots,K\}. \tag{18}$$

To handle (15c), an additional auxiliary variable $z_k > 0$ is introduced such that

$$\mathbf{a}_k^{\mathrm{T}}\mathbf{H}_{r,k}\mathbf{a}_k \leq z_k, \quad k\in\{1,\ldots,K\} \tag{19}$$

and $t_k z_k \leq u_k$. For any $\alpha_k^{(q-1)} > 0$, the arithmetic-geometric mean inequality gives $t_k z_k \leq \frac{1}{2}\left(\alpha_k^{(q-1)}t_k^2 + \frac{z_k^2}{\alpha_k^{(q-1)}}\right)$. By setting $\alpha_k^{(q-1)} = \frac{z_k^{(q-1)}}{t_k^{(q-1)}}$,the upper bound is tight and first-order consistent at the current feasible point. Therefore, the constraint $t_k z_k \leq u_k$ is conservatively approximated by

$$\frac{1}{2}\left(\alpha_k^{(q-1)}t_k^2 + \frac{z_k^2}{\alpha_k^{(q-1)}}\right) \leq u_k, \quad k\in\{1,\ldots,K\}. \tag{20}$$

Combining (18), (19), and (20) with the previously derived first-order lower bounds for the DWED terms, the AIRS-RCM update at the q^{th} SCA iteration is formulated as:

$$\mathbf{P5} \min_{\{\mathbf{a}_k,t_k,u_k,z_k\},\mathbf{v}_0} \sum_{k=1}^{K}(\tau_k \times (t_k \times SNR_{\text{threshold}} + SNR_{\text{threshold}} \times u_k + \sigma_1^2 \mathbf{a}_k^{\text{T}} \mathbf{I}_M \mathbf{a}_k + M \times P_{\text{irs}})) - \tau_0 \eta \times f(\mathbf{v}_0, \mathbf{v}_0^{q-1}) + \tau_0 \times \mathbf{v}_0^{\text{H}} \mathbf{G}_0 \mathbf{v}_0 \quad (21a)$$

$$\text{s.t.} \quad z_k > 0 \quad (21b)$$

$$(11c), (11d), (15b), (15e), (18), (19), (20). \quad (21c)$$

The objective function of **(P5)** is convex. In addition, the left-hand side of (21a) is a convex quadratic-over-linear function, whereas its right-hand side is affine. Constraints (18) and (19) are also convex. Hence, **(P5)** is a convex optimization problem and can be efficiently solved by CVX. More importantly, the approximations in (21a), (15e), and (18) constitute inner approximations that are tight and first-order consistent at the current feasible point, which is essential for establishing the convergence properties of the SCA procedure.

4.2 Optimizing the Sink Transmit and Receive Beamformers

After removing the terms independent of the beamforming variables, **(P6)** can be reformulated as:

$$\mathbf{P6} \min_{\{\boldsymbol{\omega}_k\},\boldsymbol{\omega}_0} E_{\text{ULcon}} + E_{\text{DLcon}} - E_{\text{har}} \quad (22a)$$

$$\text{s.t.} \quad \frac{\sigma_1^2 ||\boldsymbol{\omega}_k^{\text{H}} \mathbf{g} \boldsymbol{\Phi}_k||^2 + \sigma_2^2 ||\boldsymbol{\omega}_k||^2}{|\boldsymbol{\omega}_k^{\text{H}} (\mathbf{h}_{d,k} + \mathbf{g} \boldsymbol{\Phi}_k \mathbf{h}_{r,k})|^2} \times SNR_{\text{threshold}} \times ||\boldsymbol{\Phi}_k \mathbf{h}_{r,k}||^2 + \sigma_1^2 ||\boldsymbol{\Phi}_k \mathbf{I}_M||^2 \le P_{\text{out}}, \forall k \in \{1, \ldots, K\}, \quad (22b)$$

$$P_{\text{S}} ||\boldsymbol{\Phi}_0 \mathbf{g}^{\text{H}} \boldsymbol{\omega}_0||^2 + \sigma_1^2 ||\boldsymbol{\Phi}_0 \mathbf{I}_M||^2 \le P_{\text{out}}, \quad (22c)$$

$$||\boldsymbol{\omega}_k||^2 \le 1, \quad \forall k \in \{1, \ldots, K\}, \quad (22d)$$

$$||\boldsymbol{\omega}_0||^2 \le 1. \quad (22e)$$

Let $\mathbf{h}_k = \mathbf{h}_{d,k} + \mathbf{g} \boldsymbol{\Phi}_k \mathbf{h}_{r,k}$, $\mathbf{G}_k = \mathbf{g} \boldsymbol{\Phi}_k$, $h_{rk} = ||\boldsymbol{\Phi}_k \mathbf{h}_{r,k}||^2$, $I_k = \sigma_1^2 ||\boldsymbol{\Phi}_k \mathbf{I}_M||^2$, $\mathbf{G}_1 = \boldsymbol{\Phi}_0 \mathbf{g}^{\text{H}}$, $h_{rn} = \sigma_1^2 ||\mathbf{h}_{r,n}^{\text{H}} \boldsymbol{\Phi}_0||^2$, $I_0 = \sigma_1^2 ||\boldsymbol{\Phi}_0 \mathbf{I}_M||^2$, and $\mathbf{h}_n = \mathbf{h}_{d,n}^{\text{H}} + \mathbf{h}_{r,n}^{\text{H}} \boldsymbol{\Phi}_0 \mathbf{g}^{\text{H}}$. Similar to problem (**P2**), when the receive SNR threshold $SNR_{\text{threshold}}$ is fixed, the numerator of the objective function (22a) is a constant term and is independent of the optimization variables $\{\boldsymbol{\omega}_k, \boldsymbol{\omega}_0\}$. Therefore, maximizing the system EE of the EH-CRSNs can be transformed into minimizing E_{total}. After removing the terms independent of the beamforming variables, (**P6**) can be reformulated as (**P7**) at the bottom of this page.

However, problem (**P7**) remains non-convex because of the fractional objective and the quadratic coupling among the beamforming variables. According to [40], to expose the quadratic structure of the beamforming variables, define $\mathbf{A}_k = \sigma_1^2 \mathbf{G}_k \mathbf{G}_k^{\text{H}} + \sigma_2^2 \mathbf{I}_{N_{\text{t}}}$, $\mathbf{H}_k = \mathbf{h}_k \mathbf{h}_k^{\text{H}}$, $\mathbf{B} = P_{\text{S}} \mathbf{G}_1^{\text{H}} \mathbf{G}_1$, and $\mathbf{C} = \tau_0 \eta \sum_{n=1}^{N} P_{\text{S}} \mathbf{h}_n^{\text{H}} \mathbf{h}_n$. Using these definitions, **(P7)**

$$\mathbf{P7} \min_{\{\boldsymbol{\omega}_k\},\boldsymbol{\omega}_0} \sum_{k=1}^{K} (\tau_k \times (\frac{\sigma_1^2 ||\omega_k^{\text{H}} \mathbf{G}_k||^2 + \sigma_2^2 ||\boldsymbol{\omega}_k||^2}{|\boldsymbol{\omega}_k^{\text{H}} \mathbf{h}_k|^2} \times SNR_{\text{threshold}} + \frac{\sigma_1^2 ||\omega_k^{\text{H}} \mathbf{G}_k||^2 + \sigma_2^2 ||\boldsymbol{\omega}_k||^2}{|\boldsymbol{\omega}_k^{\text{H}} \mathbf{h}_k|^2} \times SNR_{\text{threshold}} \times h_{rk}) + \tau_0 (P_{\text{S}} ||\boldsymbol{\omega}_0||^2 + P_{\text{S}} ||\mathbf{G}_1 \boldsymbol{\omega}_0||^2) - \tau_0 \eta \sum_{n=1}^{N} P_{\text{S}} |\mathbf{h}_n \omega_0|^2 \quad (23a)$$

$$\text{s.t.} \quad \frac{\sigma_1^2 ||\omega_k^{\text{H}} \mathbf{G}_k||^2 + \sigma_2^2 ||\boldsymbol{\omega}_k||^2}{|\boldsymbol{\omega}_k^{\text{H}} \mathbf{h}_k|^2} \times SNR_{\text{threshold}} \times h_{rk} + I_k \le P_{\text{out}}, \ \forall k \in \{1, \ldots, K\}, \quad (23b)$$

$$P_{\text{S}} ||\mathbf{G}_1 \boldsymbol{\omega}_0||^2 + I_0 \le P_{\text{out}}, \quad (23c)$$

$$(22d), (22e). \quad (23d)$$

$$\mathbf{P8} \min_{\{\boldsymbol{\omega}_k\},\boldsymbol{\omega}_0} \sum_{k=1}^{K} (\tau_k \times (\frac{\boldsymbol{\omega}_k^{\text{H}} \mathbf{A}_k \boldsymbol{\omega}_k}{\boldsymbol{\omega}_k^{\text{H}} \mathbf{H}_k \boldsymbol{\omega}_k} \times SNR_{\text{threshold}} + \frac{\boldsymbol{\omega}_k^{\text{H}} \mathbf{A}_k \boldsymbol{\omega}_k}{\boldsymbol{\omega}_k^{\text{H}} \mathbf{H}_k \boldsymbol{\omega}_k} \times SNR_{\text{threshold}} \times h_{rk}) + \tau_0 (P_{\text{S}} \boldsymbol{\omega}_0^{\text{H}} \boldsymbol{\omega}_0 + \boldsymbol{\omega}_0^{\text{H}} \mathbf{B} \boldsymbol{\omega}_0) - \boldsymbol{\omega}_0^{\text{H}} \mathbf{C} \boldsymbol{\omega}_0 \quad (24a)$$

$$\text{s.t.} \quad \frac{\boldsymbol{\omega}_k^{\text{H}} \mathbf{A}_k \boldsymbol{\omega}_k}{\boldsymbol{\omega}_k^{\text{H}} \mathbf{H}_k \boldsymbol{\omega}_k} \times SNR_{\text{threshold}} \times h_{rk} + I_k \le P_{\text{out}}, \quad \forall k \in \{1, \ldots, K\}, \quad (24b)$$

$$\boldsymbol{\omega}_0^{\text{H}} \mathbf{B} \boldsymbol{\omega}_0 + I_0 \le P_{\text{out}}, \quad (24c)$$

$$(22d), (22e). \quad (24d)$$

can be equivalently written as **(P8)** at the bottom of the previous page. Next, introduce the lifted positive semidefinite matrices $\mathbf{W}_k = \boldsymbol{\omega}_k \boldsymbol{\omega}_k^{\mathrm{H}}$ and $\mathbf{W}_0 = \boldsymbol{\omega}_0 \boldsymbol{\omega}_0^{\mathrm{H}}$. Accordingly, $\mathrm{rank}(\mathbf{W}_k) = 1$ and $\mathrm{rank}(\mathbf{W}_0) = 1$. Using the identity $\boldsymbol{\omega}^{\mathrm{H}}\mathbf{X}\boldsymbol{\omega} = \mathrm{tr}(\mathbf{X}\mathbf{W})$, problem (P8) can be equivalently expressed as the following lifted rank-constrained formulation:

$$\begin{aligned}
\mathbf{P9} \quad & \min_{\{\mathbf{W}_k\},\mathbf{W}_0} \sum_{k=1}^{K} (\tau_k \times (\frac{\mathrm{tr}(\mathbf{A}_k\mathbf{W}_k)}{\mathrm{tr}(\mathbf{H}_k\mathbf{W}_k)} \times SNR_{\text{threshold}} \\
& + \frac{\mathrm{tr}(\mathbf{A}_k\mathbf{W}_k)}{\mathrm{tr}(\mathbf{H}_k\mathbf{W}_k)} \times SNR_{\text{threshold}} \times h_{rk})) + \tau_0(P_{\mathrm{S}}\mathrm{tr}(\mathbf{W}_0) \\
& + \mathrm{tr}(\mathbf{B}\mathbf{W}_0)) - \mathrm{tr}(\mathbf{C}\mathbf{W}_0) \qquad (25a) \\
\text{s.t.} \quad & \frac{\mathrm{tr}(\mathbf{A}_k\mathbf{W}_k)}{\mathrm{tr}(\mathbf{H}_k\mathbf{W}_k)} \times SNR_{\text{threshold}} \times h_{rk} + I_k \le P_{\text{out}}, \\
& \forall k \in \{1,\ldots,K\}, \qquad (25b) \\
& \mathrm{tr}(\mathbf{B}\mathbf{W}_0) + I_0 \le P_{\text{out}}, \qquad (25c) \\
& \mathrm{tr}(\mathbf{W}_k) \le 1, \ \ \forall k \in \{1,\ldots,K\}, \qquad (25d) \\
& \mathrm{tr}(\mathbf{W}_0) \le 1, \qquad (25e) \\
& \mathrm{rank}(\mathbf{W}_k) = 1, \ \ \forall k \in \{1,\ldots,K\}, \qquad (25f) \\
& \mathrm{rank}(\mathbf{W}_0) = 1, \qquad (25g) \\
& \mathbf{W}_k \succeq 0, \ \ \forall k \in \{1,\ldots,K\}, \qquad (25h) \\
& \mathbf{W}_0 \succeq 0. \qquad (25i)
\end{aligned}$$

where (25c) describes the total power budget constraint of AIRS in the downlink, (25e) specifies the matrix trace constraint for the squared norm of the sink's receive beamforming in the k^{th} time slot of the UDR phase, and (25i) represents the positive semidefinite matrix constraint for the sink's receive beamforming in the k^{th} time slot of the UDR phase.

Problem (**P9**) remains non-convex because of the fractional terms involving $\mathbf{W}_k$ and the rank-one constraints in (25f) and (25g). To obtain a tractable formulation, the rank-one constraints are first temporarily removed, resulting in a semidefinite relaxation of (**P9**). The remaining fractional terms associated with the UDR beamforming matrices are then handled through the Charnes-Cooper transformation. Specifically, define $p_k = 1/\mathrm{tr}(\mathbf{H}_k\mathbf{W}_k)$ and $\widetilde{\mathbf{W}}_k = p_k\mathbf{W}_k$. Since $p_k \ge 0$, the transformed variables satisfy $\mathrm{tr}(\mathbf{H}_k\tilde{\mathbf{W}}_k) = 1$. The resulting relaxed beamforming problem is:

$$\begin{aligned}
\mathbf{P10} \quad & \min_{\{\widetilde{\mathbf{W}}_k, p_k\},\mathbf{W}_0} \sum_{k=1}^{K} \Big(\tau_k \times \big(\mathrm{tr}(\mathbf{A}_k\widetilde{\mathbf{W}}_k) \times SNR_{\text{threshold}} \\
& + \mathrm{tr}(\mathbf{A}_k\widetilde{\mathbf{W}}_k) \times SNR_{\text{threshold}} \times h_{rk}\big)\Big) - \mathrm{tr}(\mathbf{C}\mathbf{W}_0) \\
& + \tau_0\big(P_{\mathrm{S}}\mathrm{tr}(\mathbf{W}_0) + \mathrm{tr}(\mathbf{B}\mathbf{W}_0)\big) \qquad (26a) \\
\text{s.t.} \quad & \mathrm{tr}(\mathbf{H}_k\widetilde{\mathbf{W}}_k) = 1, \quad \forall k \in \{1,\ldots,K\}, \qquad (26b) \\
& \mathrm{tr}(\mathbf{A}_k\widetilde{\mathbf{W}}_k) \times SNR_{\text{threshold}} \times h_{rk} + I_k \le P_{\text{out}}, \\
& \forall k \in \{1,\ldots,K\}, \qquad (26c) \\
& p_k \ge 0, \quad \forall k \in \{1,\ldots,K\}, \qquad (26d) \\
& \mathrm{tr}(\widetilde{\mathbf{W}}_k) \le p_k, \ \ \forall k \in \{1,\ldots,K\}, \qquad (26e) \\
& \widetilde{\mathbf{W}}_k \succeq 0, \ \ \forall k \in \{1,\ldots,K\}, \qquad (26f) \\
& (25c), (25e), (25i) \qquad (26g)
\end{aligned}$$

where (26b) denotes the equality constraint for $\widetilde{\mathbf{W}}_k$ scaled by p_k, (26c) represents the power amplification constraint of the AIRS in the UDR phase for $\widetilde{\mathbf{W}}_k$ scaled from (25b) by p_k, (26e) specifies the trace constraint on $\widetilde{\mathbf{W}}_k$, and (26f) is the positive semidefinite matrix constraint on $\widetilde{\mathbf{W}}_k$.

Problem (**P10**) is a convex semidefinite program and can therefore be efficiently solved using CVX. However, because the rank-one constraints have been removed in deriving (**P10**), its solution is generally only an SDR solution of (**P9**) and is not guaranteed to correspond directly to feasible beamforming vectors. Therefore, a penalty-based rank-recovery procedure is further introduced to recover numerically rank-one beamforming matrices. For any nonzero positive semidefinite matrix $\mathbf{W}$, the rank-one condition can be equivalently characterized by $\sum_{k=1}^{K}(\mathrm{tr}(\mathbf{W}) - \lambda_{\max}(\mathbf{W})) \le 0$, where $\lambda_{\max}(\mathbf{W})$ denotes the maximum eigenvalue of $\mathbf{W}$. Moreover, since $\widetilde{\mathbf{W}}_k = p_k\mathbf{W}_k$ with $p_k > 0$, positive scalar scaling does not change the matrix rank, i.e., $\mathrm{rank}(\mathbf{W}_k) = \mathrm{rank}(\widetilde{\mathbf{W}}_k)$. Therefore, the rank-one recovery of the UDR beamforming matrices can be equivalently performed on $\widetilde{\mathbf{W}}_k$, and $\mathrm{rank}(\mathbf{W}_0) = 1$ is equivalent to $\mathrm{tr}(\mathbf{W}_0) - \lambda_{\max}(\mathbf{W}_0) \le 0$. Furthermore, given the position of the AIRS, this problem is divided into 2 subproblems: minimizing the difference between the system energy consumption and the total energy gathered by all CRSN nodes during the DWED phase, and minimizing the total energy expenditure during the UDR phase. Based on the above rank-one characterization, the DWED beamforming problem can be reformulated as (**P11**).

$$\begin{aligned}
\mathbf{P11} \quad & \min_{\mathbf{W}_0} \tau_0(P_{\mathrm{S}}\mathrm{tr}(\mathbf{W}_0) + M \times P_{\text{irs}} + \mathrm{tr}(\mathbf{B}\mathbf{W}_0) \\
& + I_0) - \mathrm{tr}(\mathbf{C}\mathbf{W}_0) + p_1(\mathrm{tr}(\mathbf{W}_0) - \lambda_{\max}(\mathbf{W}_0)) \qquad (27a) \\
\text{s.t.} \quad & (25c), (25e), (25i) \qquad (27b)
\end{aligned}$$

where $p_1 > 0$ denotes the penalty factor associated with the rank-one residual $\mathrm{tr}(\mathbf{W}_0) - \lambda_{\max}(\mathbf{W}_0)$ in the DWED phase. A larger p_1 imposes a stronger penalty on the violation of the rank-one condition. However, the maximum-eigenvalue term $\lambda_{\max}(\mathbf{W}_0)$ in (**P11**) is convex, making the penalized objective non-convex. Let $\mathbf{W}_0^r$ denote the solution obtained at the r^{th} iteration and $\mathbf{u}_{\max}(\mathbf{W}_0^r)$ denote the unit-norm eigenvector associated with its maximum eigenvalue. By the first-order property of a convex function, $\lambda_{\max}(\mathbf{W}_0)$ admits the following global affine lower bound: $\lambda_{\max}(\mathbf{W}_0) \ge \mathbf{u}_{\max}(\mathbf{W}_0^r)^{\mathrm{H}}\mathbf{W}_0\mathbf{u}_{\max}(\mathbf{W}_0^r)$. The equality holds at $\mathbf{W}_0 = \mathbf{W}_0^r$. Therefore, $\mathrm{tr}(\mathbf{W}_0) - \mathbf{u}_{\max}(\mathbf{W}_0^r)^{\mathrm{H}}\mathbf{W}_0\mathbf{u}_{\max}(\mathbf{W}_0^r)$ provides a convex upper approximation of the rank-penalty term in (**P11**), which is tight at the current iterate. Accord-

ingly, (**P11**) can be iteratively solved through the following convex problem (**P12**):

$$\mathbf{P12} \quad \min_{\mathbf{W}_0} \tau_0(P_{\mathrm{S}}\mathrm{tr}(\mathbf{W}_0) + M \times P_{\mathrm{irs}} + \mathrm{tr}(\mathbf{B}\mathbf{W}_0) + I_0) - \mathrm{tr}(\mathbf{C}\mathbf{W}_0) + p_1(\mathrm{tr}(\mathbf{W}_0) - \mathbf{u}_{\max}(\mathbf{W}_0^r)^{\mathrm{H}}\mathbf{W}_0\mathbf{u}_{\max}(\mathbf{W}_0^r)) \tag{28a}$$

$$\text{s.t.} \quad (25c), (25e), (25i). \tag{28b}$$

Similarly, the rank-one constraint associated with the UDR beamforming matrices can be handled by applying the same penalty-based approach to $\widetilde{\mathbf{W}}_k$. Accordingly, the UDR beamforming problem is reformulated as (**P13**).

$$\mathbf{P13} \min_{\{\widetilde{\mathbf{W}}_k, p_k\}} \sum_{k=1}^{K} (\tau_k \times (\mathrm{tr}(\mathbf{A}_k\widetilde{\mathbf{W}}_k) \times SNR_{\mathrm{threshold}} + \mathrm{tr}(\mathbf{A}_k\widetilde{\mathbf{W}}_k) \times SNR_{\mathrm{threshold}} \times h_{rk} + I_k + M \times P_{\mathrm{irs}})) + p_2 \sum_{k=1}^{K} (\mathrm{tr}(\widetilde{\mathbf{W}}_k) - \lambda_{\max}(\widetilde{\mathbf{W}}_k)) \tag{29a}$$

$$\text{s.t.} \quad (26b), (26c), (26d), (26e), (26f) \tag{29b}$$

where $p_2 > 0$ is the penalty factor for minimizing $\sum_{k=1}^{K}(\mathrm{tr}(\mathbf{W}_k) - \lambda_{\max}(\mathbf{W}_k))$ during the UDR phase. Similarly, at the j^{th} iteration, the convexity of $\lambda_{\max}(\widetilde{\mathbf{W}}_k)$ gives $\lambda_{\max}(\widetilde{\mathbf{W}}_k) \geq \mathbf{u}_{\max}(\widetilde{\mathbf{W}}_k^j)^{\mathrm{H}}\widetilde{\mathbf{W}}_k\mathbf{u}_{\max}(\widetilde{\mathbf{W}}_k^j)$, where $\mathbf{u}_{\max}(\widetilde{\mathbf{W}}_k^j)$ is the unit-norm eigenvector corresponding to the maximum eigenvalue of $\widetilde{\mathbf{W}}_k^j$. Based on this global affine lower bound, (**P13**) can be iteratively approximated by the following convex problem (**P14**).

$$\mathbf{P14} \quad \min_{\{\widetilde{\mathbf{W}}_k\, p_k\}} \sum_{k=1}^{K} (\tau_k \times (\mathrm{tr}(\mathbf{A}_k\widetilde{\mathbf{W}}_k) \times SNR_{\mathrm{threshold}} + \mathrm{tr}(\mathbf{A}_k\widetilde{\mathbf{W}}_k) \times SNR_{\mathrm{threshold}} \times h_{rk} + I_k + M \times P_{\mathrm{irs}})) + p_2 \sum_{k=1}^{K} (\mathrm{tr}(\widetilde{\mathbf{W}}_k) - \mathbf{u}_{\max}(\widetilde{\mathbf{W}}_k^j)^{\mathrm{H}}\widetilde{\mathbf{W}}_k\mathbf{u}_{\max}(\widetilde{\mathbf{W}}_k^j)) \tag{30a}$$

$$\text{s.t.} \quad (26b), (26c), (26d), (26e), (26f). \tag{30b}$$

Problems (**P12**) and (**P14**) are convex and can be efficiently solved using CVX. The corresponding penalty-based procedures are performed iteratively by updating the dominant eigenvectors using the solutions obtained in the preceding iterations. Since the affine lower bounds of the maximum-eigenvalue functions are tight at the current iterates, the resulting surrogate penalty terms preserve the objective values at the corresponding expansion points. The convergence properties of the penalty-based rank-recovery procedures are formally established in Sec. 4.3.

Based on the above analysis, the proposed AO framework alternately updates the AIRS RCMs and sink beamformers by solving the corresponding subproblems. The overall procedure for solving (**P1**) is summarized in Algorithm 1, while the penalty-based rank-one recovery procedure employed in Step 2 of Alg. 1 is detailed in Algorithm 2.

Algorithm 1. Alternating optimization for problem (**P1**).

1: **Initialization**: Randomly generate feasible AIRS RCMs $\mathbf{\Phi}_k^0$, $\mathbf{\Phi}_0^0$, the sink beamformers $\boldsymbol{\omega}_k^0$, $\boldsymbol{\omega}_0^0$, set the initial iteration number $i = 0$, convergence accuracy $\varepsilon > 0$, and maximum iteration number I_{maxIter}. The objective function (8a) is denoted as $h(\mathbf{\Phi}_k, \mathbf{\Phi}_0, \boldsymbol{\omega}_k, \boldsymbol{\omega}_0)$, and $h(\mathbf{\Phi}_k^0, \mathbf{\Phi}_0^0, \boldsymbol{\omega}_k^0, \boldsymbol{\omega}_0^0)$ is calculated.

2: **Repeat**

3: $i = i + 1$

4: **Step 1**: Initialize the iteration count of the SCA algorithm at $q = 0$, maximum iteration number I_{maxSCA}, and convergence accuracy $\varepsilon_3 > 0$. Given the sink transmit beamformer $\boldsymbol{\omega}_0^{i-1}$ and the receive beamformer $\boldsymbol{\omega}_k^{i-1}$ in the k^{th} time slot. By selecting the feasible point $\mathbf{a}_k^0$, $\mathbf{v}_0^0$, $t_k^0 = \frac{\sigma_1^2(\mathbf{a}_k^0)^{\mathrm{T}}\mathbf{G}\mathbf{a}_k^0 + \sigma_2^2\bar{\omega}_k}{\left|\left|\bar{h}_{d,k}\right| + \bar{\mathbf{b}}_k^{\mathrm{T}}\mathbf{a}_k^0\right|^2}$, $u_k^0 = t_k^0 \times (\mathbf{a}_k^0)^{\mathrm{T}}\mathbf{H}_{r,k}\mathbf{a}_k^0$, the objective function (21a) is denoted as $g(\mathbf{a}_k, t_k, u_k, \mathbf{v}_0)$, and $g(\mathbf{a}_k^0, t_k^0, u_k^0, \mathbf{v}_0^0)$ is calculated.

5: **Repeat**

6: $q = q + 1$.

7: By solving problem (**P5**) at the given feasible point $\mathbf{a}_k^{q-1}, t_k^{q-1}, u_k^{q-1}, \mathbf{v}_k^{q-1}$, update the feasible point $\mathbf{a}_k^q, t_k^q, u_k^q, \mathbf{v}_k^q$.

8: Calculate the objective function $g(\mathbf{a}_k^q, t_k^q, u_k^q, \mathbf{v}_0^q)$.

9: **Until** $\left|\frac{g(\mathbf{a}_k^q, t_k^q, u_k^q, \mathbf{v}_0^q) - g(\mathbf{a}_k^{q-1}, t_k^{q-1}, u_k^{q-1}, \mathbf{v}_0^{q-1})}{g(\mathbf{a}_k^q, t_k^q, u_k^q, \mathbf{v}_0^q)}\right| \leq \varepsilon_3$ or $q > I_{\mathrm{maxSCA}}$.

The optimal AIRS RCM configuration $\mathbf{\Phi}_k^i$, $\mathbf{\Phi}_0^i$ in both the uplink and downlink is obtained.

10: **Step 2:** Given the updated AIRS RCMs $\mathbf{\Phi}_k^i$ and $\mathbf{\Phi}_0^i$, solve problem (**P10**) and apply the penalty-based rank-one recovery procedure summarized in Algorithm 2 to obtain the sink transmit beamformer $\boldsymbol{\omega}_0^i$ and receive beamformers $\boldsymbol{\omega}_k^i$.

11: Calculate the objective function $h(\mathbf{\Phi}_k^i, \mathbf{\Phi}_0^i, \boldsymbol{\omega}_k^i, \boldsymbol{\omega}_0^i)$.

12: **Until** $\left|\frac{h(\mathbf{\Phi}_k^i, \mathbf{\Phi}_0^i, \boldsymbol{\omega}_k^i, \boldsymbol{\omega}_0^i) - h(\mathbf{\Phi}_k^{i-1}, \mathbf{\Phi}_0^{i-1}, \boldsymbol{\omega}_k^{i-1}, \boldsymbol{\omega}_0^{i-1})}{h(\mathbf{\Phi}_k^i, \mathbf{\Phi}_0^i, \boldsymbol{\omega}_k^i, \boldsymbol{\omega}_0^i)}\right| \leq \varepsilon$ or $i > I_{\mathrm{maxIter}}$.

Algorithm 2. Penalty-based algorithm for solving problem (**P9**).

1: **Initialization:** Set the convergence tolerances $\varepsilon_1 > 0$, $\varepsilon_2 > 0$, the penalty factors $p_1 = 0.10$, $p_2 = 0.10$, $r = 0$, $j = 0$.

2: **Step 1:** Solve problem (**P10**) to obtain $\mathbf{W}_0^r$, $\widetilde{\mathbf{W}}_k^j$, and p_k^j.

3: **while** $\left|\mathrm{tr}(\mathbf{W}_0^r) - \lambda_{\max}(\mathbf{W}_0^r)\right| > \varepsilon_1$, **do**

4: Based on $\mathbf{u}_{\max}(\mathbf{W}_0^r)$, solve problem (**P12**) to obtain $\mathbf{W}_0^{r+1}$.

5: **if** $\left\|\mathbf{W}_0^{r+1} - \mathbf{W}_0^r\right\|_F \leq \varepsilon_1$, **then**

6: $p_1 = 2p_1$.

7: **else**

8: $r = r + 1$.

9: **end if**

10: **end while**

11: **Step 2: while** $\left|\mathrm{tr}(\widetilde{\mathbf{W}}_k^j) - \lambda_{\max}(\widetilde{\mathbf{W}}_k^j)\right| > \varepsilon_2, \forall k \in \{1, \ldots, K\}$, **do**

12: Based on $\mathbf{u}_{\max}(\widetilde{\mathbf{W}}_k^j)$, solve problem (**P14**) to obtain $\widetilde{\mathbf{W}}_k^{j+1}$ and p_k^{j+1}.

13: **if** $\left\|\widetilde{\mathbf{W}}_k^{j+1} - \widetilde{\mathbf{W}}_k^j\right\|_F \leq \varepsilon_2, \forall k \in \{1, \ldots, K\}$, **then**

14: $p_2 = 2p_2$.

15: **else**

16: $j = j + 1$.

17: **end if**

18: **end while**

19: **Output:** The rank-one solution $\mathbf{W}_0^r$ of the beamforming matrix for the DWED phase in problem (**P9**), and the rank-one solutions of the beamforming matrices for the UDR phase, given by $\mathbf{W}_k^j = \widetilde{\mathbf{W}}_k^j / p_k^j$.

4.3 Convergence Analysis

4.3.1 Convergence Analysis of the SCA Algorithm

Let the optimization variables at the q-1$^{\text{th}}$ iteration be denoted as $(\mathbf{a}_k^{q-1}, t_k^{q-1}, u_k^{q-1}, \mathbf{v}_0^{q-1})$. Given the linear approximations in (12) and (20), $(\mathbf{a}_k^{q-1}, t_k^{q-1}, u_k^{q-1}, \mathbf{v}_0^{q-1})$ remains feasible for the convexified problem in the q^{th} iteration. According to (21a), the surrogate function $f(\mathbf{v}_0, \mathbf{v}_0^{q-1})$ and its original function $f(\mathbf{v}_0) = \sum_{n=1}^{N}\left(P_s\left|\overline{h}_{d,n} + \mathbf{b}_n^{\mathrm{H}}\mathbf{v}_0\right|^2 + \sigma_1^2\mathbf{v}_0^{\mathrm{H}}\mathbf{H}_{r,n}\mathbf{v}_0 + \sigma_{3,n}^2\right)$ satisfy the following mathematical relation:

$$f(\mathbf{v}_0^q) \geq f(\mathbf{v}_0^q, \mathbf{v}_0^{q-1}). \tag{31}$$

When maximizing the surrogate function $f(\mathbf{v}_0, \mathbf{v}_0^{q-1})$, the obtained maximum value is no less than the value from the previous iteration; hence, the following inequality holds:

$$f(\mathbf{v}_0^q, \mathbf{v}_0^{q-1}) \geq f(\mathbf{v}_0^{q-1}, \mathbf{v}_0^{q-1}). \tag{32}$$

Since $f(\mathbf{v}_0^{q-1}, \mathbf{v}_0^{q-1})$ is the Taylor expansion of the original function at $\mathbf{v}_0^{q-1}$, we have:

$$f(\mathbf{v}_0^{q-1}, \mathbf{v}_0^{q-1}) = f(\mathbf{v}_0^{q-1}). \tag{33}$$

From (31)–(33), we can obtain the following chain of inequalities:

$$f(\mathbf{v}_0^{q-1}) = f(\mathbf{v}_0^{q-1}, \mathbf{v}_0^{q-1}) \leq f(\mathbf{v}_0^q, \mathbf{v}_0^{q-1}) \leq f(\mathbf{v}_0^q). \tag{34}$$

From (34), it follows that $f(\mathbf{v}_0^{q-1}) \leq f(\mathbf{v}_0^q)$, which proves the monotonic non-decreasing property of the original function throughout the iterations. Therefore, it can be deduced that $g(\mathbf{a}_k^q, t_k^q, u_k^q, \mathbf{v}_0^q) \leq g(\mathbf{a}_k^{q-1}, t_k^{q-1}, u_k^{q-1}, \mathbf{v}_0^{q-1})$. This indicates that the objective function value of the SCA algorithm is non-decreasing. Given the restriction on the AIRS APB, the objective function $g(\mathbf{a}_k, t_k, u_k, \mathbf{v}_0)$ has an lower limit, thereby guaranteeing the algorithm's convergence.

4.3.2 Convergence of the Penalty-Based Rank-Recovery Procedure

To tackle the non-convex rank-one constraint $\mathrm{rank}(\mathbf{W}) = 1$, we exploit the algebraic property of positive semidefinite matrices. For any non-zero matrix $\mathbf{W} \succeq \mathbf{0}$, the rank-one condition is equivalent to

$$\mathrm{tr}(\mathbf{W}) - \lambda_{\max}(\mathbf{W}) = 0 \tag{35}$$

where $\lambda_{\max}(\mathbf{W})$ denotes the maximum eigenvalue of $\mathbf{W}$. Accordingly, we define the non-negative rank-one residual function as

$$\phi(\mathbf{W}) = \mathrm{tr}(\mathbf{W}) - \lambda_{\max}(\mathbf{W}). \tag{36}$$

By incorporating $\phi(\mathbf{W})$ as a penalty term into the objective function, the rank-constrained optimization problem is reformulated into a penalized problem:

$$\min_{\mathbf{W}\in\mathcal{W}} F_\rho(\mathbf{W}) = f_0(\mathbf{W}) + \rho\,\phi(\mathbf{W}) \tag{37}$$

where $\mathcal{W}$ denotes the convex feasible set, $f_0(\mathbf{W})$ is the convex objective function, and $\rho > 0$ represents the penalty factor.

Note that problem (37) is still non-convex because $-\lambda_{\max}(\mathbf{W})$ is a concave function with respect to $\mathbf{W}$. To overcome this challenge, the SCA framework is applied. Since $\lambda_{\max}(\mathbf{W})$ is convex, its first-order Taylor expansion at the current iterate $\mathbf{W}^{(l)}$ provides a global affine lower bound:

$$\begin{aligned}\lambda_{\max}(\mathbf{W}) &\geq \lambda_{\max}\left(\mathbf{W}^{(l)}\right) + \mathrm{tr}\left[\mathbf{u}_{\max}^{(l)}(\mathbf{u}_{\max}^{(l)})^H\left(\mathbf{W} - \mathbf{W}^{(l)}\right)\right] \\ &= \underline{\lambda}_{\max}\left(\mathbf{W} \mid \mathbf{W}^{(l)}\right)\end{aligned} \tag{38}$$

where $\mathbf{u}_{\max}^{(l)}$ is the normalized eigenvector corresponding to $\lambda_{\max}\left(\mathbf{W}^{(l)}\right)$, satisfying $\|\mathbf{u}_{\max}^{(l)}\|_2 = 1$ and $\mathbf{W}^{(l)}\mathbf{u}_{\max}^{(l)} = \lambda_{\max}\left(\mathbf{W}^{(l)}\right)\mathbf{u}_{\max}^{(l)}$. Substituting the identity $\mathbf{u}_{\max}^{(l)H}\mathbf{W}^{(l)}\mathbf{u}_{\max}^{(l)} = \lambda_{\max}\left(\mathbf{W}^{(l)}\right)$ into (38) yields

$$\underline{\lambda}_{\max}\left(\mathbf{W} \mid \mathbf{W}^{(l)}\right) = (\mathbf{u}_{\max}^{(l)})^H\mathbf{W}\mathbf{u}_{\max}^{(l)}. \tag{39}$$

Consequently, a convex (affine) upper surrogate function for the rank-one residual $\phi(\mathbf{W})$ is constructed as

$$\widetilde{\phi}\left(\mathbf{W} \mid \mathbf{W}^{(l)}\right) = \mathrm{tr}(\mathbf{W}) - (\mathbf{u}_{\max}^{(l)})^H\mathbf{W}\mathbf{u}_{\max}^{(l)}. \tag{40}$$

At iteration $l+1$, with a fixed penalty factor ρ, the updated matrix $\mathbf{W}^{(l+1)}$ is obtained by solving the following convex semidefinite program:

$$\begin{aligned}\mathbf{W}^{(l+1)} &= \arg\min_{\mathbf{W}\in\mathcal{W}} \widetilde{F}_\rho\left(\mathbf{W} \mid \mathbf{W}^{(l)}\right) \\ &= \arg\min_{\mathbf{W}\in\mathcal{W}} f_0(\mathbf{W}) + \rho\,\widetilde{\phi}\left(\mathbf{W} \mid \mathbf{W}^{(l)}\right).\end{aligned} \tag{41}$$

For any fixed penalty parameter $\rho > 0$, the sequence of penalized objective values $\{F_\rho(\mathbf{W}^{(l)})\}$ generated by iteratively solving (41) is monotonically non-increasing and converges. According to (38) and (40), the upper surrogate function satisfies two key properties:

$$\phi(\mathbf{W}) \leq \widetilde{\phi}\left(\mathbf{W} \mid \mathbf{W}^{(l)}\right), \quad \forall\,\mathbf{W} \in \mathcal{W}, \tag{42}$$

$$\phi\left(\mathbf{W}^{(l)}\right) = \widetilde{\phi}\left(\mathbf{W}^{(l)} \mid \mathbf{W}^{(l)}\right). \tag{43}$$

Since $\mathbf{W}^{(l+1)}$ is the optimal solution to the convex subproblem (41), we have the following chain of inequalities:

$$\begin{aligned} F_\rho\left(\mathbf{W}^{(l+1)}\right) &\leq \widetilde{F}_\rho\left(\mathbf{W}^{(l+1)} \mid \mathbf{W}^{(l)}\right) \\ &\leq \widetilde{F}_\rho\left(\mathbf{W}^{(l)} \mid \mathbf{W}^{(l)}\right) \\ &= F_\rho\left(\mathbf{W}^{(l)}\right). \end{aligned} \tag{44}$$

Because physical constraints guarantee that the objective function is bounded from below, the monotone convergence theorem ensures that the inner iteration sequence $F_\rho\left(\mathbf{W}^{(l+1)}\right)$ converges to a stationary point. From the above derivation, it can be seen that problems (**P12**) and (**P14**) are monotonically non-decreasing and bounded from above, which proves that Convergence of the Penalty-Based Rank-Recovery.

4.3.3 Convergence Analysis of the AO Algorithm

Let $\{\mathbf{\Phi}_0, \mathbf{\Phi}_k, \boldsymbol{\omega}_0, \boldsymbol{\omega}_k\}$ denote the variables after the i-th overall AO iteration. The corresponding objective value of the system energy efficiency is defined as:

$$EE^{(i)} = EE\left(\mathbf{\Phi}_0^{(i)}, \mathbf{\Phi}_k^{(i)}, \boldsymbol{\omega}_0^{(i)}, \boldsymbol{\omega}_k^{(i)}\right). \tag{45}$$

First, by fixing the beamforming vectors $\{\boldsymbol{\omega}_0^{(i-1)}, \boldsymbol{\omega}_k^{(i-1)}\}$ to update the AIRS reflection matrices $\{\mathbf{\Phi}_0, \mathbf{\Phi}_k\}$, according to the fundamental properties of the SCA algorithm, the constructed surrogate function strictly satisfies the first-order consistency and global lower-bounding properties at the current expansion point. Solving the convex surrogate subproblem guarantees that the original objective value is monotonically non-decreasing:

$$\begin{aligned} &EE\left(\mathbf{\Phi}_0^{(i)}, \mathbf{\Phi}_k^{(i)}, \boldsymbol{\omega}_0^{(i-1)}, \boldsymbol{\omega}_k^{(i-1)}\right) \\ &\geq EE\left(\mathbf{\Phi}_0^{(i-1)}, \mathbf{\Phi}_k^{(i-1)}, \boldsymbol{\omega}_0^{(i-1)}, \boldsymbol{\omega}_k^{(i-1)}\right). \end{aligned} \tag{46}$$

Then, by fixing the AIRS reflection matrices $\{\mathbf{\Phi}_0^{(i)}, \mathbf{\Phi}_k^{(i)}\}$ to update the beamforming vectors $\{\boldsymbol{\omega}_0, \boldsymbol{\omega}_k\}$, the newly generated beamforming vectors are accepted only if they do not decrease the current system energy efficiency; otherwise, the solution from the previous iteration is retained. Therefore, it holds that:

$$EE\left(\mathbf{\Phi}_0^{(i)}, \mathbf{\Phi}_k^{(i)}, \boldsymbol{\omega}_0^{(i)}, \boldsymbol{\omega}_k^{(i)}\right) \geq EE\left(\mathbf{\Phi}_0^{(i)}, \mathbf{\Phi}_k^{(i)}, \boldsymbol{\omega}_0^{(i-1)}, \boldsymbol{\omega}_k^{(i-1)}\right). \tag{47}$$

Define the intermediate half-step iteration value as:

$$EE^{\left(i-\frac{1}{2}\right)} = EE\left(\mathbf{\Phi}_0^{(i)}, \mathbf{\Phi}_k^{(i)}, \boldsymbol{\omega}_0^{(i-1)}, \boldsymbol{\omega}_k^{(i-1)}\right). \tag{48}$$

Combining (B1) and (B2), the following monotonic relationship holds in any i-th overall iteration:

$$EE^{(i-1)} \leq EE^{\left(i-\frac{1}{2}\right)} \leq EE^{(i)}. \tag{49}$$

Therefore, the sequence of objective function values $\{EE^{(i)}\}$ generated by the algorithm is monotonically non-decreasing.Additionally, due to the limitations imposed by the sink's TP and the AIRS APB, and both the channel gains and allocated bandwidth B across all wireless links are finite. According to Shannon's formula, the total achievable rate of the system has an upper bound, i.e., $R_{\text{total}} \leq R_{\max} < \infty$. Moreover, considering the static circuit loss and basic component power dissipation, the net energy consumption of the system E_{sys} strictly remains positive within the considered operational region. According to (8a), the system energy efficiency has a finite upper bound $EE_{\max}$:

$$EE^{(i)} \leq EE_{\max} < \infty, \quad \forall i. \tag{50}$$

This completes the proof of the monotonicity and convergence of the proposed AO algorithm.

4.4 Analysis of Algorithm Complexity

To solve the optimization problem (**P1**), this paper applies the SCA algorithm to optimize the AIRS RCMs in both uplink and downlink and uses the SDR technique to optimize the sink transmit and receive beamformers. Hence, the algorithm's primary computational complexity lies in resolving the optimization problems (**P5**), (**P10**), (**P12**), and (**P14**). Specifically, if the cumulative count of iterations of the SCA algorithm is I_{maxSCA}, according to [15], the approximate computational complexity associated with updating $(K+1) \times M + 2K$ variables using the SCA algorithm is $O(I_{\text{maxSCA}}((K+1) \times M + 2K)^3)$. Problem (**P10**) is a semidefinite programming (SDP) problem subject to $4K+3$ constraints involving positive semidefinite matrices of dimension N_{t} and $2K$ constraints involving positive semidefinite matrices of dimension 1. Its approximate computational complexity is given by $O\big(\log(1/\epsilon)\big((4K+3)(N_{\text{t}}^{3.5} + (4K+3)N_{\text{t}}^{2.5} + (4K+3)^2 N_{\text{t}}^{0.5}) + (2K)(1+2K+(2K)^2)\big)\big)$, where ϵ denotes the solution accuracy of the SDP problem. Let I_{maxui} denote the maximum number of iterations for problem (**P12**); its approximate computational complexity, which is subject to 3 constraints involving positive semidefinite matrices of dimension N_{t}, is $O\big(I_{\text{maxui}}\big(\log(1/\epsilon)(3(N_{\text{t}}^{3.5} + 3N_{\text{t}}^{2.5} + 3^2 N_{\text{t}}^{0.5}))\big)\big)$. Let I_{maxup} denote the maximum number of iterations for problem (**P14**); its approximate computational complexity, which is subject to $4K$ constraints involving positive semidefinite matrices of dimension N_{t} and $2K$ constraints involving positive semidefinite matrices of dimension 1, is $O\big(I_{\text{maxup}}\big(\log(1/\epsilon)\big((4K)(N_{\text{t}}^{3.5} + (4K)N_{\text{t}}^{2.5} + (4K)^2 N_{\text{t}}^{0.5}) + (2K)(1+2K+(2K)^2)\big)\big)\big)$. Let I_{maxIter} denote the total number of iterations of the AO algorithm; then the overall computational complexity of the proposed algorithm is expressed as $O\Big(I_{\text{maxIter}}\Big(I_{\text{maxSCA}}\big((K+1)M+2K\big)^3 + \log(1/\epsilon)\Big((4K+3)\big(N_{\text{t}}^{3.5} + (4K+3)N_{\text{t}}^{2.5} + (4K+3)^2 N_{\text{t}}^{0.5}\big) + 2K\big(1+2K+(2K)^2\big)\Big) + I_{\text{maxui}}\log(1/\epsilon)\Big(3\big(N_{\text{t}}^{3.5} + 3N_{\text{t}}^{2.5} + 3^2 N_{\text{t}}^{0.5}\big)\Big) + I_{\text{maxup}}\log(1/\epsilon)\Big(4K\big(N_{\text{t}}^{3.5} + 4KN_{\text{t}}^{2.5} + (4K)^2 N_{\text{t}}^{0.5}\big) + 2K\big(1+2K+(2K)^2\big)\Big)\Big)\Big)$.

Parameters	Values
Reference path loss C_0	-32 dB
Rician factors β_{IS}, β_{CI}, and β_{CS}	2
Path-loss exponent of AIRS-sink link α_{IS}	2.3
CH-AIRS link Path-loss exponent of CH k-AIRS link α_{CI}	2.3
Path-loss exponent of CH k-sink link α_{CS}	2.9
Static noise power σ_1^2, σ_2^2, and $\sigma_{3,n}^2$	-80 dBm
Network radius A	50 m
Total number of CRSNs nodes N	100
Number of clusters K	20
Number of antennas equipped at the sink N_{t}	4
Maximum transmit power of the sink P_{S}	40 dBm
Time duration of EH τ_0	0.5 s
Uplink data reporting duration of CH k τ_k	0.001 s
Conversion efficiency of EH circuits η	0.8
Power consumption of the switch and control circuits at each RE P_{C}	-10 dBm
Power consumption of DC biasing at each RE P_{DC}	-10 dBm
Energy consumption of electronic circuitry per bit E_{elec}	50 nJ/bit
Energy consumption for data aggregation per bit E_{DA}	5 nJ/bit/packet
Data packet size L	1000 bits
Energy dissipation coefficient of power amplifier in free-space model $\varepsilon_{\mathrm{fs}}$	10 pJ/bit/m^2
Energy dissipation coefficient of power amplifier in multipath fading model $\varepsilon_{\mathrm{mp}}$	0.0013 pJ/bit/m^4
Threshold distance d_0	87.7 m
Vertical distance between AIRS and x-y plane H_{IRS}	5 m
Channel bandwidth B	100 kHz
SNR threshold $SNR_{\mathrm{threshold}}$	30 dB

Tab. 2. Simulation parameter settings.

5. Simulation Analysis and Performance Verification

All channels are modeled as Rician fading channels. Accordingly, the equivalent baseband channel $\mathbf{g}$ for the AIRS-sink link can be expressed as:

$$\mathbf{g} = \sqrt{\mathrm{C}_0\left(\frac{d_{\mathrm{IS}}}{D_0}\right)^{-\alpha_{\mathrm{IS}}}} \times \left(\sqrt{\frac{\beta_{\mathrm{IS}}}{1+\beta_{\mathrm{IS}}}}\mathbf{g}^{\mathrm{LoS}} + \sqrt{\frac{1}{1+\beta_{\mathrm{IS}}}}\mathbf{g}^{\mathrm{NLoS}}\right), \tag{51}$$

where the reference path loss is set to $C_0 = -32$ dB at $D_0 = 1$ m, We sincerely appreciate the reviewer's valuable comments. The reference distance D_0 is an artificially configured standard normalization reference point used to compute the reference free-space path loss C_0. While d_{IS}, α_{IS}, and β_{IS} stand for the AIRS-sink distance, the path-loss exponent, and the Rician factor. The line-of-sight and scattered components of this link are represented by $\mathbf{g}^{\mathrm{LoS}}$ and $\mathbf{g}^{\mathrm{NLoS}}$, where $\mathbf{g}^{\mathrm{NLoS}}$ is generated according to independent Rayleigh fading. The channels for the CRSN node n-AIRS link and the CRSN node n-sink link are produced in the same fashion. The above parameters are all adopted from [10]. The convergence accuracy for the AO algorithm, SCA algorithm, and penalty-based algorithm is 10^{-3}. In practical active reflecting circuits, P_{DC} is not strictly constant. To provide a higher reflection amplitude gain while maintaining the amplifier operating within its linear region, dynamically adjusting the DC bias voltage/current is often required, which implies that higher gains are typically accompanied by an increased P_{DC}. Similarly, P_{C} depends on the phase shifter architecture; due to differing bias currents in the ON and OFF switching states, P_{C} may fluctuate across different discrete phase states. To achieve an analytically tractable yet practically representative power consumption model, the values of $P_{\mathrm{C}}$and P_{DC} are selected according to the parameter settings reported in [41] and [42]. Unless otherwise specified, the remaining simulation parameters are adopted from [12] and listed in Tab. 2. The simulation parameter settings in Tab. 2 are configured as follows: The threshold distance d_0 is a critical physical distance determined by the crossover point between the free-space loss and the multipath fading loss in the first-order radio energy consumption model, where $d_0 = \sqrt{\varepsilon_{\mathrm{fs}}/\varepsilon_{\mathrm{mp}}}$. Specifically, when the transmission distance is less than d_0, the free-space path loss model is adopted to quantify signal attenuation; when the transmission distance is greater than or equal to d_0, the two-ray ground-reflection path loss model is employed instead. $SNR_{\mathrm{threshold}}$ is the minimum received SNR required for receiver demodulation. The network comprises N CRSN nodes randomly distributed within a circular area of radius A, which are partitioned into K clusters. The AIRS is deployed at a vertical altitude of H_{IRS} above the x-y plane, and the sink node is equipped with N_{t} antennas, subject to a maximum transmit power constraint P_{S}. The channel bandwidth is B. The path loss exponents for the AIRS-sink link, the link between the CH$_k$ and the AIRS, and the CH$_k$-sink link are denoted as α_{IS}, αCI, and αCS, respectively, with the corresponding Rician factors denoted as β_{IS}, βCI, and βCS. The static thermal noise powers at the AIRS, the sink, and CRSN node n are represented by σ_1^2, σ_2^2, and $\sigma_{3,n}^2$, respectively. The transmission frame is divided into a DWED duration τ_0 with an energy harvesting conversion efficiency of η, and UDR durations τ_k for each CH$_k$ to transmit packets of size L. Regarding node energy consumption, we adopt the classic

first-order radio model, which encompasses the electronics energy dissipation E_{elec}, data aggregation energy E_{DA}, and power amplifier coefficients ε_{fs} and ε_{mp}.

All numerical simulations were performed on a computer equipped with an Intel Core i5-12600KF CPU and 32 GB of RAM, running Windows 10. The proposed optimization algorithm was implemented in MATLAB R2022b, and the convex optimization problems were solved using CVX 2.2 with the Mosek solver. No GPU or additional hardware acceleration was used in our simulations. To assess its EE performance, the following benchmark schemes are considered:

- 1) Joint energy delivery and data reporting scheme for PIRS-aided EH-CRSNs (referred to as PIRS): The PIRS uses the optimal RCM configuration for both UDR and DWED, with the reflection amplitude set to 1, and the sink always employs the optimal beamformers. To ensure fairness, the PIRS is assigned a total power budget $P_{\text{IRS}} = 9.2$ dBm, corresponding to the quantity of active REs $M = 10$. In this scenario, the quantity of passive REs is 83.

- 2) Joint energy delivery and data reporting scheme for AIRS-aided single-input single-output EH-CRSNs (referred to as ASingle): The sink is equipped with a single antenna, and the AIRS utilizes the optimal RCM configuration for both UDR and DWED.

- 3) Energy delivery and data reporting scheme for maximizing NEG in AIRS-aided EH-CRSNs (referred to as AEbenefit) [10]: The system's NEG is defined as the difference between the total energy gathered by all CRSN nodes and the energy consumption of CHs during UDR. This scheme aims to maximize the system's NEG by jointly optimizing the sink transmit and receive beamformers and the AIRS RCM.

- 4) UDR scheme for maximizing NEG in AIRS-aided EH-CRSNs (referred to as AUplink) [43]: The AIRS utilizes the optimal RCM configuration for assisting time-division UDR and a randomly selected RCM that meets the constraints for assisting DWED. The sink which is configured with multiple antennas always adopts the optimal beamforming configuration.

- 5) DWED scheme for AIRS-aided EH-CRSNs (referred to as ADownlink): The AIRS adopts the optimal RCM configuration for DWED and a randomly selected RCM that meets the constraints for assisting UDR. The sink always maintains the optimal beamforming configuration.

- 6) Random energy delivery and data reporting scheme for AIRS-aided EH-CRSNs (referred to as ARandom): The AIRS is configured with a random RCM that meets the constraints for both UDR and DWED, while the sink consistently applies the optimal beamforming configuration.

- 7) Downlink-oriented energy delivery and data reporting scheme for AIRS-aided EH-CRSNs (referred to as AUnified): The AIRS adopts the optimal RCM for DWED when assisting both UDR and DWED, while the sink consistently maintains the optimal beamforming configuration.

- 8) Energy delivery and data reporting scheme for EH-CRSNs without IRS assistance (referred to as NIRS): the sink-node interaction is supported exclusively by direct wireless links, while the sink consistently adopts the optimal beamforming configuration.

Additionally, the proposed design aims to maximize system EE by jointly optimizing the AIRS RCMs in both uplink and downlink and the sink transmit and receiver beamformers while satisfying the uplink and downlink APB constraints for the AIRS. As indicated by (8a) and (8b), the system EE is closely related to the APB P_{out} of the AIRS and the amount of active REs M. Therefore, this study explores how changes in these parameters impact system EE, providing guidance for future parameter configurations in AIRS-aided EH-CRSNs.

5.1 Effectiveness Validation of the Proposed Joint Design

Under the adopted parameter setting, the AIRS location yielding the largest system EE is found to be (0,2.1,5). This position is therefore used in the subsequent simulations. Additionally, because the first dead node appears at different rounds under different energy delivery and data reporting schemes, a common observation window is adopted for comparison, specifically from the beginning of network operation until the first dead node appears in the NIRS scheme. Without IRS assistance, the NIRS benchmark provides weaker support for DWED and requires higher energy consumption during UDR. Accordingly, the remaining energy of CRSN nodes decreases fastest in the NIRS scheme, causing the first dead node to appear the earliest. The system EE in each round is influenced by the quantity of CHs selected by CogLEACH protocol in that round. When the count of clusters increases, the energy consumption for UDR also increases, resulting in a decrease in system EE. Because the count of CHs selected by CogLEACH varies from round to round, the system EE values are sampled every 310 rounds to make the cross-scheme comparison more transparent. The specific results are presented in Fig. 3, where the quantity of CHs selected in each round is 18, 10, 19, and 21, respectively.

Figure 3 shows that the proposed design achieves the highest system EE among the compared schemes, with the order of system EE from highest to lowest being: the proposed design, AUplink, ADownlink, ARandom, PIRS, AUnified, NIRS, AEbenefit, and ASingle. However, when the quantity of CHs is relatively small, the system EE under the PIRS scheme can be lower than that under the NIRS scheme. The observed performance differences can be understood from

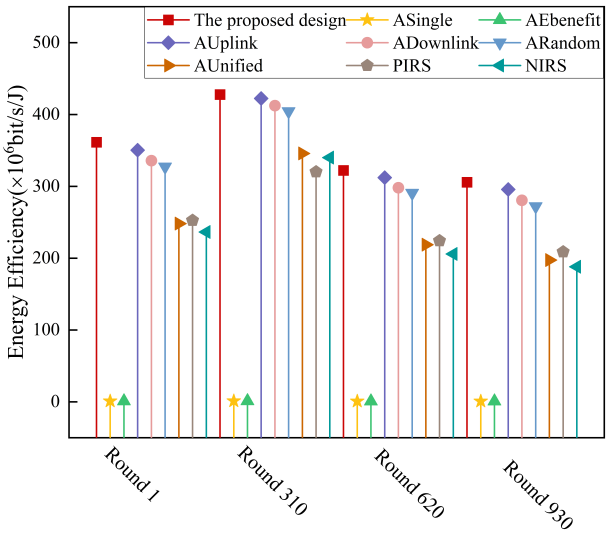


Fig. 3. System EE comparison of the EH-CRSNs across different schemes.

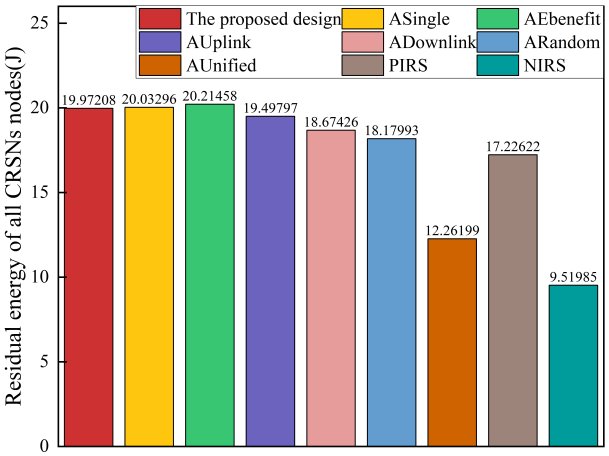


Fig. 4. Total remaining energy of all CRSN nodes at the point when the first node dies.

the following aspects. From (9a), the total achievable rate R_{total} in this paper is a constant value. Therefore, maximizing the system EE is equivalent to minimizing the system's total energy expenditure E_{total}.

- 1) The EE advantage of the proposed design comes from the coordinated optimization of the AIRS RCMs in the DWED and UDR phases together with the sink transmit and receive beamformers. Since the downlink energy cost still accounts for a large portion of the total system expenditure, the harvested energy of all CRSN nodes cannot completely offset this consumption. When balancing between minimizing system energy consumption and maximizing the overall energy gathered, the AIRS RCM configuration tends to prioritize energy consumption reduction. The adjustment of the sink transmit beamformer reduces system energy consumption while slightly diminishing the total energy gathered by all nodes, resulting in the remaining energy of the CRSN nodes being slightly lower than in the AEbenefit and ASingle schemes. The overall residual energy of all CRSN nodes is detailed in Fig. 4.

- 2) The lower system EE of AUplink, ADownlink, and ARandom is mainly due to the lack of jointly optimized AIRS RCMs across the DWED and UDR phases. As a result, these schemes cannot fully exploit the AIRS amplification capability, which weakens either DWED, UDR, or both. As a result, the system EE and the remaining energy of the CRSN nodes are lower in these 3 schemes than in the proposed design. Additionally, since UDR is the dominant phase, the remaining energy of the CRSN nodes is particularly low in the ADownlink and ARandom schemes, where the optimal AIRS RCM configuration for the uplink is not considered. This is especially true for the ARandom scheme, where both the uplink and downlink AIRS RCMs are randomly configured.

- 3) Unlike AIRS, PIRS can only reflect the incident signal and cannot provide amplitude amplification. Consequently, the cascaded link remains strongly constrained by the multiplicative-fading effect. Under the same total IRS power budget and the same SNR requirement at the sink, the CHs in the PIRS scheme must transmit with higher power during the UDR phase compared to the AIRS-aided schemes mentioned above, leading to higher system energy consumption. Additionally, CRSN nodes obtain less energy during the DWED phase, resulting in lower residual energy for the nodes. Furthermore, since the PIRS is configured with 83 REs, the energy consumption during the DWED phase is higher than in the AIRS-aided schemes, leading to lower EE in the PIRS scheme. However, when the count of clusters is small, the energy consumption for CHs in UDR is relatively low. The PIRS scheme must account for the static energy consumption of the PIRS in the cascaded reflection link for both uplink and downlink, whereas the total system energy expenditure in the NIRS scheme only includes the energy expenditure of the sink and CRSN nodes. Consequently, the total energy consumption in the PIRS scheme is slightly higher than that in the NIRS scheme, leading to slightly lower EE.

- 4) As noted in [9], when the TP is low, the AIRS is less affected by the APB constraint. However, as the TP increases, the APB constraint becomes more pronounced and restricts the AIRS's amplification gain. In the DWED phase, the sink's TP is relatively high, leading to a reduced amplitude amplification gain for the AIRS in the AUnified scheme. When the AIRS RCM optimized for the downlink is applied to UDR, it cannot effectively reduce the system energy consumption in the uplink, resulting in lower EE. Therefore, the remaining energy of the CRSN nodes in this scheme is also relatively low.

- 5) Both the AEbenefit and ASingle schemes fail to effectively reduce the energy consumption of the cascaded IRS reflection link in both uplink and downlink,

resulting in higher total system energy consumption. Specifically, the AEbenefit scheme focuses on maximizing the system NEG by optimizing wireless energy delivery efficiency while reducing the energy required by CHs for UDR. Consequently, CRSN nodes in this scheme have the highest remaining energy. However, this scheme does not account for the energy expenditure of the AIRS and sink during the optimization process, and the AIRS RCM and beamformer configured to maximize NEG cannot effectively reduce E_{total}, resulting in lower system EE. The ASingle scheme seeks to reduce total system energy consumption solely through optimizing the AIRS RCMs in both uplink and downlink. Despite all CRSN nodes collecting substantial energy, the sink's energy consumption in the DWED phase remains high, and with the sink equipped with only a single antenna, it is unable to reduce energy expenditure through active beamforming. Likewise, the sink cannot fully leverage active beamforming in the UDR phase, leading to the lowest EE in this scheme. In the NIRS scheme, the total system energy consumption only includes that of the sink and CRSN nodes, leading to lower overall energy consumption and higher EE compared to the 2 schemes mentioned above. These simulation outcomes indicate that under an identical total IRS power budget, the AIRS-aided EH-CRSNs exhibit superior EE compared to the PIRS-aided systems, provided that the uplink and downlink beamformers are jointly optimized.

To evaluate the robustness of the proposed joint design against channel estimation errors, we consider an imperfect-CSI scenario in which $\mathbf{h}$ denotes the estimated CSI available for optimization, while the actual channel is modeled as $\mathbf{h} + \Delta\mathbf{h}$, where $\Delta\mathbf{h}$ denotes the channel estimation error. Since the considered system involves the IRS-sink, CH k-IRS, and CH k-sink links with different channel dimensions and average channel gains, the channel estimation error is characterized in a normalized form. Specifically, the normalized channel estimation error is defined as the ratio of the channel estimation error to the corresponding estimated channel norm and follows a circularly symmetric complex Gaussian distribution $\mathcal{CN}(0, \delta)$. The same normalized error level is considered for the three types of links, while the estimation errors are independently generated. For each channel realization, the proposed joint optimization is first performed using the estimated CSI $\mathbf{h}$ to obtain the optimization variables. These variables are then applied to the actual channel $\mathbf{h} + \Delta\mathbf{h}$ to calculate the resulting system energy consumption and EE. Therefore, the considered simulation setup explicitly characterizes the performance degradation caused by the mismatch between the CSI used for optimization and the actual propagation channels.

Figure 5(a) shows the system EE of different schemes under normalized channel estimation errors. As δ increases, the mismatch between the estimated CSI used for optimization and the actual propagation channels becomes more pronounced, resulting in different degrees of EE degradation. For the proposed joint design, when δ increases from 0 to 0.2, the system EE decreases by only 0.15768%. Moreover, the proposed joint design consistently achieves higher system EE than all the benchmark schemes over the range of channel estimation errors considered. Specifically, the proposed joint design achieves an EE improvement of at least 47.87% over the PIRS scheme. These results indicate that the EE advantage achieved by the proposed joint design is maintained in the presence of CSI estimation errors.

To further investigate the effect of channel estimation errors on the energy utilization of the different schemes, Fig. 5(b) presents the corresponding total system energy consumption. The proposed joint design consistently achieves the lowest energy consumption over the considered range of δ, and only minor variations are observed as the channel estimation error increases. In comparison, the benchmark schemes generally exhibit higher energy consumption, while some schemes show

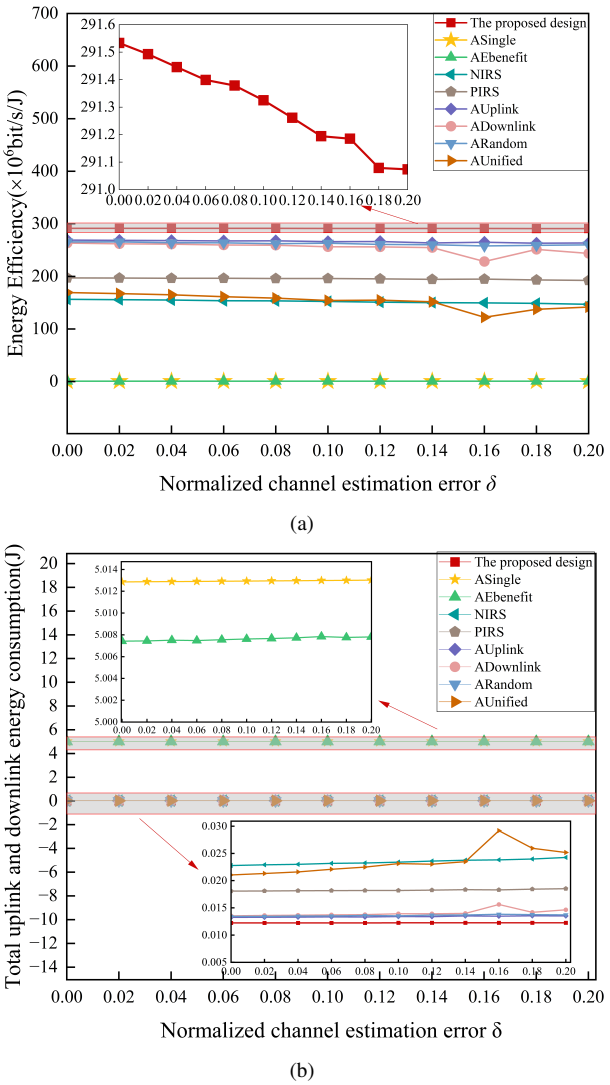


Fig. 5. Performance comparison under different normalized channel estimation errors: (a) system EE; (b) energy consumption.

more noticeable fluctuations under increasing channel estimation errors. In particular, the energy consumption of the ASingle and AEbenefit schemes remains at approximately 5 J, which is substantially higher than that of the proposed joint design and the other benchmark schemes.

Combining the results in Figs. 5(a) and 5(b), channel estimation errors introduce a mismatch between the optimization solution obtained from the estimated CSI and the actual channel conditions, thereby affecting the achievable system performance. Nevertheless, the proposed joint design maintains both a relatively stable energy-consumption level and a higher system EE than the benchmark schemes over the considered CSI-error range. Therefore, the performance advantage of the proposed joint design is not limited to the ideal CSI condition and can still be maintained under the considered imperfect-CSI conditions.

5.2 Analysis of the Impact of Key Parameters on the Performance of the Proposed Design

To examine the effect of the AIRS APB, the count of active REs is fixed at $M = 10$, and the simulation data are recorded under different values of P_{out}. The observation window starts from the beginning of network operation and ends at the round when the first dead node appears for $P_{\text{out}} = 4\,\text{dBm}$. This choice is motivated by the fact that a small P_{out} provides limited amplification capability for the AIRS. Under this condition, the CHs consume more energy during the UDR phase, while all CRSN nodes harvest less energy during the DWED phase, which causes the residual node energy to decrease faster. To compare the system EE under different APB settings, the corresponding EE values are sampled every 310 rounds. The associated numbers of CHs are 18, 10, 19, and 21, respectively. The specific results are shown in Fig. 6.

Figure 6 shows that the system EE generally increases first and then decreases as P_{out} grows. In addition, when the count of CHs is small, the EE achieved at $P_{\text{out}} = 14\,\text{dBm}$ can be slightly higher than that at $P_{\text{out}} = 12\,\text{dBm}$. This trend can be explained from the following 2 aspects. 1) The APB P_{out} for the AIRS simultaneously affects both the DWED and UDR in EH-CRSNs. When P_{out} increases, the amplitude amplification of incident signals imposed by the AIRS in both the uplink and downlink is enhanced, leading to more downlink energy being collected, and reduced uplink energy consumption for CHs. As a result, the residual energy of all CRSN nodes increases, as depicted in Fig. 7. During the UDR phase, the AIRS can reduce the TP of CHs, thereby decreasing the system energy expenditure and improving the system EE. However, while the AIRS amplifies the power of the incident signal, it also amplifies the noise power. An excessively large P_{out} leads to an increase in noise power, resulting in higher energy consumption for CHs during UDR and a reduction in residual energy. Additionally, an increase in P_{out} raises the energy expenditure of the AIRS itself, thereby reducing the system EE. 2) When the count of clusters is small, the energy consumption for UDR is low. As P_{out} increases, the system EE still shows an initial rise followed by a decline. When P_{out} becomes large enough, the influence of the DWED phase on system EE strengthens. This results in lower system energy consumption in the downlink and more harvested energy, leading to an enhancement in the system EE in the case of $P_{\text{out}} = 14\,\text{dBm}$ compared with that in the case of $P_{\text{out}} = 12\,\text{dBm}$.

Next, the AIRS APB is fixed at $P_{\text{out}} = 8\,\text{dBm}$, and the count of active REs is varied to evaluate its impact on system EE. The observation window spans from the beginning of network operation to the round at which the first dead node appears when $M = 5$. This setting is adopted because, under a fixed P_{out}, a smaller number of active REs leads to weaker AIRS beamforming capability. Consequently, the CHs require more energy for UDR, and the CRSN nodes obtain less energy during DWED, which causes the first dead node to appear earlier. To compare the EE under different values of M, the corresponding EE values are recorded every 310 rounds. The associated numbers of CHs are 18, 10, 19, and 14, respectively. The detailed outcomes are depicted in Fig. 8.

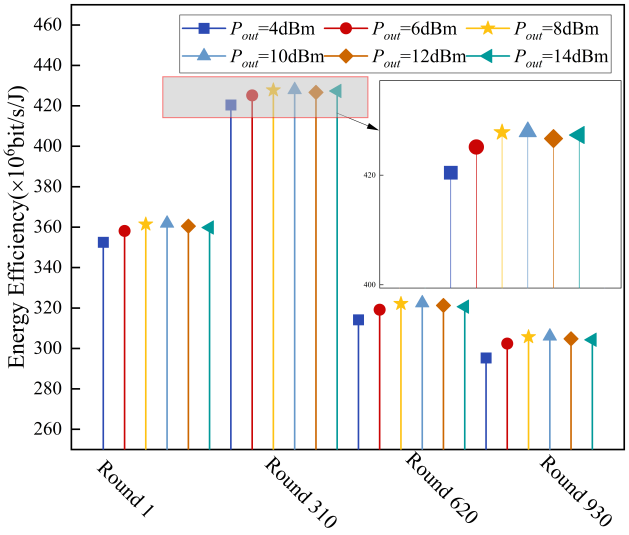


Fig. 6. The impact of P_{out} on the system EE.

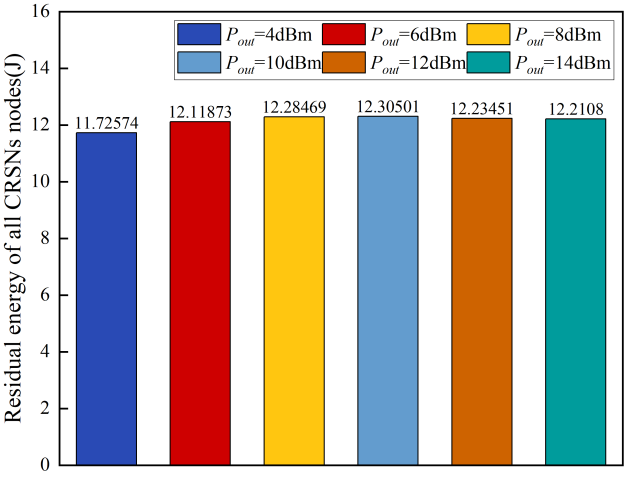


Fig. 7. Total remaining energy of all CRSN nodes under various APB Pout for the AIRS.

Figure 8 shows that the system EE also follows a rise-then-fall trend as M increases. Moreover, when the count of CHs is small, the highest EE can be achieved at $M = 5$. The detailed reasons are: 1) The variation in M affects both the DWED and UDR of CRSN nodes. As M increases, all CRSN nodes harvest more downlink energy, and the uplink and downlink energy consumption decreases, leading to an increase in system EE and a gradual rise in the residual energy of CRSN nodes, as illustrated in Fig. 9. However, as M increases, the uplink and downlink energy expenditure of the AIRS also rises. When M becomes too large, the increased system energy consumption in the uplink and downlink leads to a decline in system EE. 2) When the quantity of clusters is small, the energy consumption for CHs' UDR is relatively low, and the uplink system energy expenditure mainly depends on the energy expenditure of the AIRS. Under the condition that the APB for AIRS remains unchanged, a smaller number of active REs M leads to lower energy expenditure of the AIRS, resulting in higher system EE.

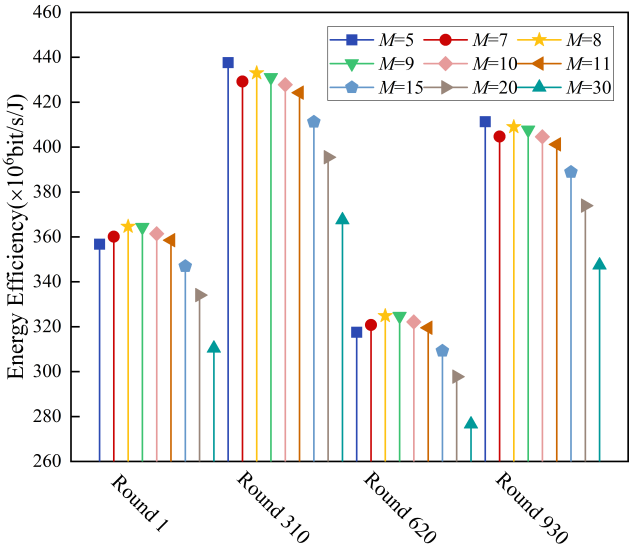


Fig. 8. The impact of the quantity of active REs M on the system EE.

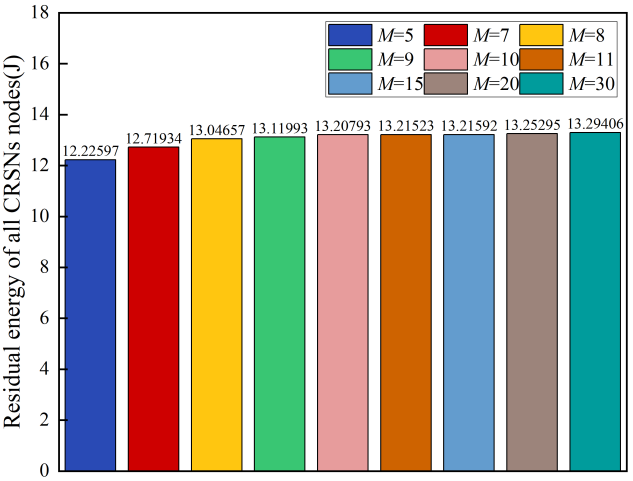


Fig. 9. Total remaining energy of all CRSN nodes under various number of active REs.

To further verify the effectiveness of the proposed joint design under more practical propagation conditions, we additionally consider a scenario in which the direct sink-CH k link experiences severe blockage, the CH is located in a NLoS region, or no dominant LoS path exists. Therefore, throughout the simulations, the direct sink-CH k link is modeled as a flat Rayleigh fading channel, where the small-scale fading coefficients are modeled as independent and identically distributed circularly symmetric complex Gaussian random variables distributed as $\mathcal{CN}(0, 1)$, while all the other simulation parameters remain unchanged. The corresponding simulation results are presented in Fig. 10.

The results demonstrate that, even under the considered Rayleigh fading scenario, the EE of the AIRS-aided EH-CRSNs employing the proposed joint design remains higher than those of all the benchmark schemes, achieving an EE improvement of at least 8.6%. Moreover, compared with the original Rician fading scenario with a dominant LoS component, the performance advantage of the proposed joint design over the benchmark schemes becomes more pronounced.

To provide a clearer comparison of the system EE between the proposed joint design and the PIRS scheme, we have conducted additional simulations under an identical reflecting-element configuration. Specifically, both the AIRS and PIRS are equipped with 10 reflecting elements, while all other simulation parameters remain unchanged. The corresponding results are provided in Fig. 11.

As shown in Fig. 11, under the same RE configuration, for different numbers of CHs, the system EE achieved by the proposed joint design is consistently higher than that of the PIRS scheme. The system EE achieved by the proposed joint design is at least 34.64% higher than that achieved by the PIRS scheme, thereby validating the effectiveness of the AIRS.

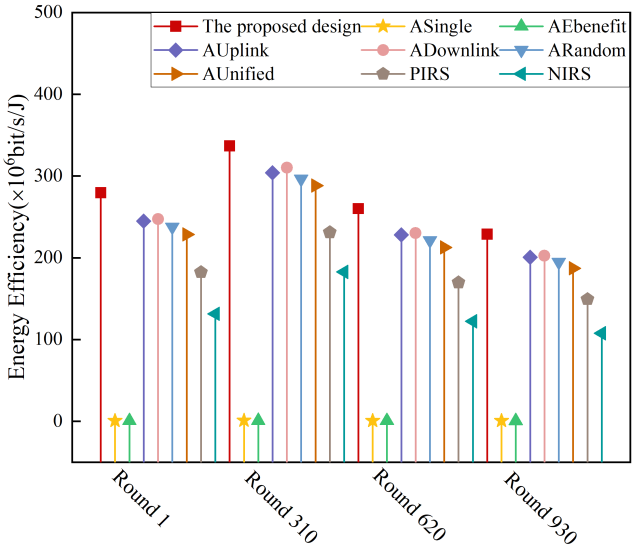


Fig. 10. System EE comparison of different schemes for EH-CRSNs under Rayleigh fading.

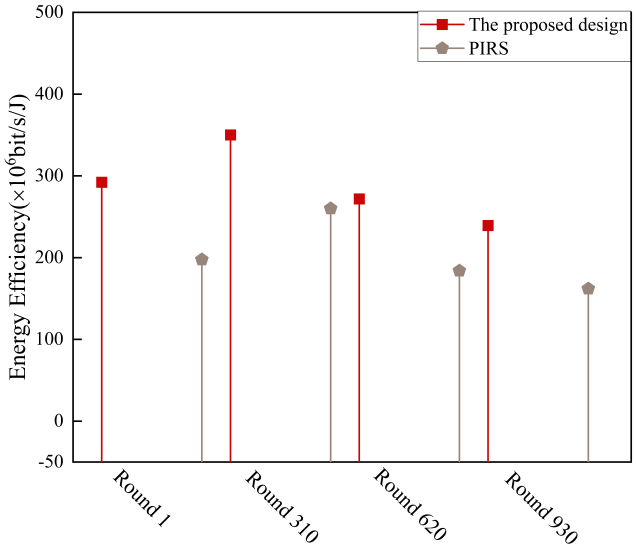


Fig. 11. Comparison of system EE between the proposed joint design and the PIRS scheme for EH-CRSNs with an equal number of REs.

6. Conclusions

This paper has investigated the system-level EE design for AIRS-aided EH-CRSNs, taking perfect instantaneous CSI as the benchmark to systematically quantify the theoretical performance limits and ultimate gain upper bounds achievable by the system. A joint optimization framework was developed for the sink transmit beamformer in the DWED phase, the sink receive beamformer in the UDR phase, and the AIRS RCMs adopted in the 2 phases under the sink power constraint and the AIRS APBs. To handle the resulting nonconvex problem, an AO framework combining SCA and SDR was employed. The numerical results confirm that the proposed design can substantially improve system EE over the benchmark schemes, while maintaining the reduction in the residual energy of CRSN nodes within a small range. The simulations also reveal that the APB of the AIRS and the count of active REs play a critical role in the EE performance of AIRS-aided EH-CRSNs. Increasing either of them does not always lead to better performance, since inappropriate parameter settings may introduce excessive AIRS-side energy consumption and thus reduce the overall system EE. The optimization framework developed in this work is based on the estimated CSI available to the system. Additional simulations under imperfect CSI show that channel estimation errors lead to a mismatch between the optimization solution obtained from the estimated CSI and the actual propagation channels, resulting in performance degradation. Nevertheless, the proposed joint design maintains its EE advantage over the benchmark schemes within the considered range of channel estimation errors. In AIRS-assisted EH-CRSNs, explicitly incorporating CSI uncertainty into the problem formulation leads to intricate high-order coupling among channel estimation errors, AIRS dynamic amplified noise, and active power budget constraints. This may require resorting to the S-Procedure or Bernstein-type inequality to reformulate the existing framework into tractable forms, such as SDP. Developing a robust joint optimization framework that explicitly incorporates CSI uncertainty into the problem formulation will be considered in future work. In addition, the count of sink antennas is fixed in this work, and its joint impact on system EE has not been explored. These issues will be considered in future research on EE-oriented design for AIRS-aided EH-CRSNs.

It should be noted that the adopted AIRS power-consumption model characterizes P_{C} and P_{DC} as fixed per-element parameters following existing studies. Their actual values may depend on the circuit architecture, operating state, and hardware configuration of a practical AIRS. Therefore, the current model provides a system-level abstraction rather than a hardware-calibrated power model. Developing and validating a more detailed AIRS power-consumption model based on practical hardware measurements will be considered in future work.

Acknowledgments

This research was funded by the National Natural Science Foundation of China under Grant 61901102 and the Science and Technology Development Plan Project of Jilin City under Grant 20240103052.

Data Availability

The MATLAB source code used to generate the numerical results presented in this paper is publicly available at: https://github.com/xq3468-code/vndsf.

References

[1] ERGUL, O., ALAGOZ, F., AKAN, O. B. Throughput maximization in electromagnetic energy harvesting cognitive radio sensor networks. *International Journal of Communication Systems*, 2016, vol. 29, no. 7, p. 1305–1322. DOI: 10.1002/dac.3100

[2] FERNANDO, X., LAZAROIU, G. Spectrum sensing, clustering algorithms, and energy-harvesting technology for cognitive-radio-based Internet-of-Things networks. *Sensors*, 2023, vol. 23, no. 18, p. 1–19. DOI: 10.3390/s23187792

[3] WASIF, S., ISHTIAQ, A., WASEEM, N. RE-HARP: RF energy harvesting MAC protocol to prolong life time of CRSNs. *Radioengineering*, 2018, vol. 27, no. 3, p. 899–908. DOI: 10.13164/re.2018.0899

[4] VILLALONGA, D. A. U., GÓMEZ, J. T., GARCÍA, M. J. F.-G. Optimal sensing policy for energy harvesting cognitive radio systems. *IEEE Transactions on Wireless Communications*, 2020, vol. 19, no. 6, p. 3826–3838. DOI: 10.1109/TWC.2020.2978818

[5] ÖZDOGAN, Ö., BJÖRNSON, E., LARSSON, E. G. Intelligent reflecting surfaces: Physics, propagation, and pathloss modeling. *IEEE Wireless Communications Letters*, 2020, vol. 9, no. 5, p. 581–585. DOI: 10.1109/LWC.2019.2960779

[6] PAN, C. H., ZONE, G., ZHI, K. D., et al. An overview of signal processing techniques for RIS/IRS-aided wireless systems. *IEEE Journal of Selected Topics in Signal Processing*, 2022, vol. 16, no. 5, p. 883–917. DOI: 10.1109/JSTSP.2022.3195671

[7] BENAYA, A. M., HASSAN, M. S., ISMAIL, M. H., et al. Double-faced active intelligent reflecting surfaces-assisted symbiotic radio communications. *IEEE Open Journal of Vehicular Technology*, 2024, vol. 5, p. 577–591. DOI: 10.1109/OJVT.2024.3384102

[8] LE-THANH, T., TRAN-MINH, C., HO-VAN, K. Active IRS-aided NOMA with full-duplex energy harvesting wire-tapper: Performance evaluation. *Computer Communications*, 2026, vol. 246, p. 1–12. DOI: 10.1016/j.comcom.2025.108372

[9] LONG, R. Z., LIANG, Y. C., PEI, Y. Y., et al. Active reconfigurable intelligent surface-aided wireless communications. *IEEE Transactions on Wireless Communications*, 2021, vol. 20, no. 8, p. 4962–4975. DOI: 10.1109/TWC.2021.3064024

[10] WANG, J. H., ZHU, Y. N. Joint passive beamforming and deployment design for active intelligent reflecting surface-assisted energy harvesting-cognitive radio sensor networks. *Scientific Reports*, 2024, vol. 14, no. 1, p. 1–18. DOI: 10.1038/s41598-024-75349-6

[11] LU, J. R., LAI, S. W., XIA, J. J., et al. Performance analysis for IRS-assisted MEC networks with unit selection. *Physical Communications*, 2022, vol. 55, p. 1–20. DOI: 10.1016/j.phycom.2022.101869

[12] ZHAO, F., HAO, W. M., YOU, X. B., et al. Joint beamforming optimization for IRS-aided THz communication with time delays. *IEEE Wireless Communications Letters*, 2024, vol. 13, no. 1, p. 49–53. DOI: 10.1109/LWC.2023.3319347

[13] QIU, C., WU, Q. Q., HUA, M., et al. Achieving multi-beam gain in intelligent reflecting surface assisted wireless energy transfer. *IEEE Transactions on Vehicular Technology*, 2023, vol. 72, no. 3, p. 4052–4057. DOI: 10.1109/TVT.2022.3215627

[14] WANG, J. H., YU, H. Q. RF energy harvesting schemes for intelligent reflecting surface-aided cognitive radio sensor networks. *Scientific Reports*, 2022, vol. 12, p. 1–12. DOI: 10.1038/s41598-022-26853-0

[15] ZHAO, L., QU, S. C., XU, H. B., et al. Energy-efficient trajectory design for secure SWIPT systems assisted by UAV-IRS. *Vehicular Communications*, 2024, vol. 45, p. 1–10. DOI: 10.1016/j.vehcom.2023.100725

[16] ZARGARI, S., HAKIMI, A., TELLAMBURA, C., et al. User scheduling and trajectory optimization for energy-efficient IRS-UAV networks with SWIPT. *IEEE Transactions on Vehicular Technology*, 2023, vol. 72, no. 2, p. 1815–1830. DOI: 10.1109/TVT.2022.3207700

[17] GOKTAS, M. B., DURSUN, Y., DING, Z. G. IRS and SWIPT-assisted full-duplex NOMA for 6G umMTC. *IEEE Transactions on Green Communications and Networking*, 2023, vol. 7, no. 4, p. 1957–1970. DOI: 10.1109/TGCN.2023.3289505

[18] WU, Q. Q., ZHANG, R. Weighted sum power maximization for intelligent reflecting surface aided SWIPT. *IEEE Wireless Communications Letters*, 2020, vol. 9, no. 5, p. 586–590. DOI: 10.1109/LWC.2019.2961656

[19] LI, Z. D., CHEN, W., WU, Q. Q., et al. Joint beamforming design and power splitting optimization in IRS-assisted SWIPT NOMA networks. *IEEE Transactions on Wireless Communications*, 2022, vol. 21, no. 3, p. 2019–2033. DOI: 10.1109/TWC.2021.3108901

[20] TANG, J., PENG, Z. Y., SO, D. K. C., et al. Energy efficiency optimization for a multiuser IRS-aided MISO system with SWIPT. *IEEE Transactions on Communications*, 2023, vol. 71, no. 10, p. 5950–5962. DOI: 10.1109/TCOMM.2023.3296631

[21] XIE, W. W., LI, Y. X., YU, C., et al. Sum rate maximization for self-sustainable IRS-assisted UAV communications. *IEEE Communications Letters*, 2023, vol. 27, no. 2, p. 640–644. DOI: 10.1109/LCOMM.2022.3223876

[22] WANG, W. H., GONG, Y. S., YANG, L., et al. Robust resource allocation design for secure IRS-aided WPCN. *IEEE Transactions on Wireless Communications*, 2023, vol. 22, no. 4, p. 2715–2729. DOI: 10.1109/TWC.2022.3213544

[23] MAO, S., LIU, L., ZHANG, N., et al. Resource scheduling for intelligent reflecting surface-assisted full-duplex wireless-powered communication networks with phase errors. *IEEE Internet of Things Journal*, 2023, vol. 10, no. 7, p. 6018–6030. DOI: 10.1109/JIOT.2022.3224533

[24] ZHOU, Y., JIN, Z. Q., SHI, H. G., et al. Flying IRS: QoE-driven trajectory optimization and resource allocation based on adaptive deployment for WPCNs in 6G IoT. *IEEE Internet of Things Journal*, 2024, vol. 11, no. 5, p. 9031–9046. DOI: 10.1109/JIOT.2023.3322266

[25] ZHAI, L. S., ZOU, Y. L., ZHU, J. Stackelberg game-based multiple access design for intelligent reflecting surface assisted wireless powered IoT networks. *IEEE Transactions on Wireless Communications*, 2023, vol. 22, no. 10, p. 6883–6897. DOI: 10.1109/TWC.2023.3246561

[26] SYAM, M. S., LUO, S., CHE, Y. L., et al. Energy-efficient intelligent reflecting surface aided wireless-powered IIoT networks. *IEEE Systems Journal*, 2022, vol. 17, no. 2, p. 2534–2545. DOI: 10.1109/JSYST.2022.3186964

[27] JI, T. T., HUA, M., LI, C. G., et al. Exploiting intelligent reflecting surface for enhancing full-duplex wireless-powered communication networks. *IEEE Transactions on Communications*, 2024, vol. 72, no. 1, p. 553–569. DOI: 10.1109/TCOMM.2023.3323532

[28] LU, Z. P., YUE, X. W., CHEN, S., et al. Outage behaviors of active intelligent reflecting surface enabled NOMA communications. *Computer Modeling in Engineering and Sciences*, 2023, vol. 137, no. 1, p. 789–812. DOI: 10.32604/cmes.2023.027663

[29] DONG, L. M., WANG, H. M., BAI, J. L. Active reconfigurable intelligent surface aided secure transmission. *IEEE Transactions on Vehicular Technology*, 2022, vol. 71, no. 2, p. 2181–2186. DOI: 10.1109/TVT.2021.3135498

[30] WANG, M. L., XU, Z., XIA, B., et al. Active intelligent reflecting surface aided covert communications. *IEEE Transactions on Vehicular Technology*, 2023, vol. 72, no. 4, p. 5401–5406. DOI: 10.1109/TVT.2022.3224024

[31] QIAO, T. T., CAO, Y., TANG, J., et al. Energy efficiency maximization for active IRS-assisted uplink NOMA systems. *IEEE Wireless Communications Letters*, 2024, vol. 13, no. 6, p. 1561–1565. DOI: 10.1109/LWC.2024.3381949

[32] ZENG, P. A., QIAO, D. L., WU, Q. Q., et al. Throughput maximization for active intelligent reflecting surface-aided wireless powered communications. *IEEE Wireless Communications Letters*, 2022, vol. 11, no. 5, p. 992–996. DOI: 10.1109/LWC.2022.3152563

[33] HAMEED, I., KOO, I. Enhancing throughput in IoT networks: The impact of active RIS on wireless powered communication systems. *Electronics*, 2024, vol. 13, no. 7, p. 1–32. DOI: 10.3390/electronics13071402

[34] GAO, Y., WU, Q. Q., ZHANG, G. C., et al. Beamforming optimization for active intelligent reflecting surface-aided SWIPT. *IEEE Transactions on Wireless Communications*, 2023, vol. 22, no. 1, p. 362–378. DOI: 10.1109/TWC.2022.3193845

[35] SHI, W. P., WU, Q. Q., WU, D., et al. Joint transmit and reflective beamforming design for active IRS-aided SWIPT systems. *Chinese Journal of Electronics*, 2024, vol. 33, no. 2, p. 536–548. DOI: 10.23919/cje.2022.00.287

[36] ELETREBY, R., ELSAYED, H., KHAIRY, M. CogLEACH: A spectrum aware clustering protocol for cognitive radio sensor networks. In *9th International Conference on Cognitive Radio Oriented Wireless Networks and Communications (CROWNCOM)*. Oulu (Finland), 2014, p. 179–184. DOI: 10.4108/icst.crowncom.2014.255370

[37] ZHOU, G., PAN, C. H., REN, H., et al. Channel estimation for RIS-aided multiuser millimeter-wave systems. *IEEE Transactions on Signal Processing*, 2022, vol. 70, p. 1478–1492. DOI: 10.1109/TSP.2022.3158024

[38] WANG, J. H., WANG, Z. A data augmentation-based channel estimation scheme for intelligent reflecting surface-assisted wireless communication system. *IEEE Transactions on Cognitive Communications and Networking*, 2025, vol. 11, no. 2, p. 1184–1196. DOI: 10.1109/TCCN.2024.3454222

[39] HEINZELMAN, W. B., CHANDRAKASAN, A. P., BALAKRISHNAN, H. An application-specific protocol architecture for wireless microsensor networks. *IEEE Transactions on Wireless Communications*, 2002, vol. 1, no. 4, p. 660–670. DOI: 10.1109/TWC.2002.804190

[40] CHU, Z., ZHU, Z. Y., ZHOU, F. H., et al. Intelligent reflecting surface assisted wireless powered sensor networks for internet of things. *IEEE Transactions on Communications*, 2021, vol. 69, no. 7, p. 4877–4889. DOI: 10.1109/TCOMM.2021.3074539

[41] KUMAR, D., SINGH, C. K., ALCARAZ LÓPEZ, O. L., et al. Performance Analysis of Passive/Active RIS Aided Wireless-Powered IoT Network With Nonlinear Energy Harvesting. *IEEE Transactions on Wireless Communications*, 2025, vol. 24, no. 2, p. 1132–1145. DOI: 10.1109/TWC.2024.3505296

[42] ANOKYE, P., SHIN, S., BENJILLALI, M., et al. Analysis and optimization of multi-active RIS assisted cell-free massive MIMO. *IEEE Internet of Things Journal*, 2026, vol. 13, no. 11, p. 23306–23329. DOI: 10.1109/JIOT.2026.3669770

[43] CHEN, G. J., WU, Q. Q., HE, C., et al. Active IRS aided multiple access for energy-constrained IoT systems. *IEEE Transactions on Wireless Communications*, 2023, vol. 22, no. 3, p. 1677–1694. DOI: 10.1109/TWC.2022.3206332

About the Authors ...

Jihong WANG (corresponding author) was born in 1986. She received her PhD. degree in Communication and Information Systems from School of Communication Engineering, Jilin University, China, in 2016. She is currently a Full Professor with Northeast Electric Power University, Jilin, China. Her research interests include ognitive radio sensor networks, energy harvesting, physical layer security and intelligent reflecting surface.

Qiang XU was born in 2002. He received his B.S. degree in Medical Information Engineering from Northeast Electric Power University, Jilin, China, in 2024. He is currently pursuing the M.Sc. degree in Northeast Electric Power University, Jilin, China. His research interests include intelligent reflecting surface, energy harvesting, clustering routing protocol design for cognitive radio sensor networks.

Yanan ZHU was born in 2000. She received her M.Sc. degree in Medical Information Engineering from Northeast Electric Power University, Jilin, China, in 2025. Her research interests include energy harvesting, intelligent reflecting surface, clustering routing protocol design for cognitive radio sensor networks.

Yang LI was born in 1980. He received the Ph.D. degree in Electrical Engineering from North China Electric Power University, Beijing, China, in 2014. He is currently a Full Professor with the School of Northeast Electric Power University, Jilin, China. His research interests include digital sustainable energy systems, AI-driven power system stability analysis, and cybersecurity and privacy preservation.

Ikromjon Usmonovichb RAKHMONOV was born in 1987. He received the D.Sc. degree in Technical Sciences, in 2022. He is currently a Professor and the Head of the Department of Power Supply with Tashkent State Technical University, Tashkent, Uzbekistan. His research interests include industrial power supply systems, energy management, energy efficiency, electricity consumption management and optimization, intelligent control of power systems, reactive power compensation, and energy-efficient technologies for industrial enterprises.

Kahramon Rakhimovichb ALLAEV was born in 1945. He received the D.Sc. degree in 1991. He is currently an Academician of the Academy of Sciences of the Republic of Uzbekistan and a Professor with Tashkent State Technical University, Tashkent, Uzbekistan. His research interests include electric power systems, power system stability, asynchronous turbogenerators, energy efficiency, energy and resource conservation, mathematical modeling and control of power systems, transient processes in electrical systems, generator excitation control, stability enhancement, power transmission, hydropower systems, and hydraulic transient processes.